2017

Linking process-structure-property relationships: Modeling and optimization in thin film morphologies

Spencer Pfeifer
Iowa State University

Linking process-structure-property relationships: Modeling and optimization in thin film morphologies

by

Spencer Pfeifer

A dissertation submitted to the graduate faculty
in partial fulfillment of the requirements for the degree of
DOCTOR OF PHILOSOPHY

Major: Mechanical Engineering

Program of Study Committee:
Baskar Ganapathysubramanian, Major Professor
Ming-Chen Hsu
James Evans
Alberto Passalacqua
Soumik Sarkar

The student author, whose presentation of the scholarship herein was approved by the program of study committee, is solely responsible for the content of this dissertation. The Graduate College will ensure this dissertation is globally accessible and will not permit alterations after a degree is conferred.

Iowa State University
Ames, Iowa
2017

TABLE OF CONTENTS

Page

CHAPTER LIST OF FIGURES iv

ABSTRACT vii

CHAPTER 1. INTRODUCTION 1

1.1 Objectives 2

1.2 Overview 3

CHAPTER 2. AN OPTIMIZATION APPROACH TO IDENTIFY PROCESSING PATHWAYS FOR ACHIEVING TAILORED THIN FILM MORPHOLOGIES 4

2.1 Introduction 5

2.2 Morphology evolution & phase-field modeling 7

2.2.1 Phase-field model 7

2.2.2 Substrate patterning 10

2.2.3 Numerical implementation 10

2.3 Optimization 11

2.3.1 Objective function 12

2.3.2 Particle swarm 18

2.3.3 Implementation 19

2.4 Results 20

2.5 Conclusions 23

CHAPTER 3. PROCESS OPTIMIZATION FOR MICROSTRUCTURE-DEPENDENT PROPERTY MAXIMIZATION IN THIN FILM ORGANIC ELECTRONICS 28

3.1 Introduction 29

3.2 Ternary phase-field model 32

3.3 Graph-based morphology quantification . . . 33
3.4 Bayesian optimization . . . 35
3.5 Numerical Implementation . . . 36
3.6 Results & Discussion . . . 36
3.6.1 Influence of evaporation rate & substrate patterning . . . 37
3.6.2 Optimization . . . 38
3.7 Conclusions . . . 41
CHAPTER 4. CONCLUSIONS AND FUTURE WORK . . . 43
4.1 Future Work . . . 43
CHAPTER 5. BIBLIOGRAPHY . . . 45

LIST OF FIGURES

Page

Figure 2.1 Representative phase-field simulation. (a) Time evolution profiles for the *Total* (F), *Bulk* (F_{bulk}), and *Interfacial* (F_{int}) free energy components (Eqs. 2.1-2.3). (b) Two-dimensional solutions (*top-down*), sampled at several points of interest throughout the evolution. 8

Figure 2.2 Illustrative representations of microstructural evolution on a patterned substrates (*images have been truncated for visualization purposes*). Full simulations are performed on 600×60 element 2D cross sections (with only one-fourth of the domain, 150×60 shown), with $\phi_0 = 0.5238$, $\epsilon^2 = 6\text{E-}5$, and surface pattern, λ_p, applied at lower boundary, with surface potential, $h = 5\text{E-}4$. 12

Figure 2.3 (a) Illustrative representations of four typical morphologies. The *checkered* structure is induced by the substrate pattern and appears immediately after phase separation. *Disordered* and *columnar* structures appear at the later-stages and depend on the efficacy of the substrate pattern. The *layered* structure is generally present for homogeneously patterned surfaces (all attractive or all repulsive). (b) 1D autocorrelation (ACF), averaged over the three slices shown, for the *disordered* and *columnar* structures to the left. The ACF is used as a penalty function to differentiate between structures. 16

Figure 2.4 Particle Swarm Optimization (PSO) methodology. 24

Figure 2.5 (Top) The objective function evaluated across the search space. Blue points indicate the initial particle swarm positions ($N = 20$), while the red point indicates the final convergent position. (Bottom) The desired morphology, labeled $\tilde{\phi}_{target}$, and final identified morphology, labeled ϕ_{opt}. Images have been truncated for visualization purposes. The images in the insets are one-fourth of domain while the two images at the bottom show one-half of domain. 25

Figure 2.6 (Top) The objective function evaluated across the search space. Blue points indicate the initial swarm positions ($N = 20$), while the red point indicates the final convergent position. (Bottom) The desired morphology, labeled $\tilde{\phi}_{target}$, and final identified morphology, labeled ϕ_{opt}. Images have been truncated for visualization purposes. The images in the insets are one-fourth of domain while the two images at the bottom show one-half of domain. 26

Figure 2.7 (Top) The objective function evaluated across the search space. Blue points indicate the initial swarm positions ($N = 20$), while the red point indicates the final convergent position. (Bottom) The desired morphology, labeled $\tilde{\phi}_{target}$, and final identified morphology, labeled ϕ_{opt}. Images have been truncated for visualization purposes. The images in the insets are one-fourth of domain while the two images at the bottom show one-half of domain. 27

Figure 3.1 (Left) The objective function evaluated across the search space with several points of interest highlighted. Point A (blue), indicates the global maxima (optimal solution). (Right) Corresponding morphologies for points A - F (*Note: Images have been truncated for visualization purposes; only one-third of the domain length is shown*) 38

Figure 3.2 Electron and hole current densities for (a) The optimal solution predicted by the Bayesian optimization framework; and (b) Nearby, high-performing morphology. . 39

Figure 3.3 (Left) The objective function for $2\,L_d$. Here, point B (blue), indicates the global maxima (optimal solution). (Right) Corresponding morphologies for points A - F (*Note: Images have been truncated for visualization purposes; only one-third of the domain length is shown*) 40

Figure 3.4 Electron and hole current densities for $2\,L_d$ simulation; (a) The predicted optimal solution for $2\,L_d$; and (b) Previous optimal solution, predicted for L_d. 41

ABSTRACT

With the rise of the plastic electronics, there has been a renewed interest in microstructure-sensitive design. Since processing conditions are known to heavily influence the microstructure, identifying optimal fabrication conditions is a crucial step towards the development of high-performance devices. A key component of this undertaking is the integration of effective computational tools; trial-and-error methods are no longer feasible, as they are time and resource intensive. In this work, several computational tools are developed to explore the process-structure-property relationships in designing high-performance thin film devices. More specifically, a phase-field – based model, developed to simulate fabrication conditions, is coupled with advanced optimization routines to systematically identify promising processing conditions, in an automated way. Throughout this work, various processing conditions are explored and it is shown how they can be tuned to achieve a desired microstructure or device performance. The methodology presented here provides a scalable and extensible approach towards the rational design of tailored microstructures with enhanced functionalities.

CHAPTER 1. INTRODUCTION

The emerging field of *organic electronics* (OE) is steadily maturing into a preeminent industry of enormous disruptive potential. The prospect of multi-functional, *plastic* electronic devices has fueled the imaginations of researchers for decades. Now, many futuristic concepts are slowly emerging from the backgrounds of science fiction and into the consumer spotlight. The growing enthusiasm stems from the immensely attractive properties inherent to semiconducting polymer blends, which provides a remarkable competitive-advantage over their inorganic counterparts. Perhaps the most damaging, of course, is that all of the familiar electronic functionalities can be packed into an ultra-thin, lightweight, and flexible form factor [1]. In addition, and perhaps of equal importance, such devices can be sustainably produced at low-costs through established high-throughput printing processes, using biodegradable and nontoxic organic materials [2, 3, 4].

However, the scope for many organic electronic devices should not be viewed as a narrow replacement for traditional (often silicon-based) devices. Rather, much of the excitement is drawn towards a number of entirely new innovations, destined to fill previously unoccupied spaces in the marketplace, yet capable of addressing complex problems of critical interest. Examples include wearable electronics and RFID tags (a key component for the Internet of Things (IoT) paradigm [5]), which are expected to improve workplace safety, while significantly improving industrial output through increased automation. However, the rising star garnering the most attention is the broad field of bioelectronics [6, 7, 8]. These 'soft' devices are part of a rapidly growing field that encompasses a range of devices capable of interfacing with the human body. This includes stretchable sensor arrays and electronic 'smart' skin [9, 10, 11] to implantable devices, and multifunctional, integrated systems capable of interfacing with the central nervous system [12, 7].

Unfortunately, in addition to some lofty expectations, many OE devices have notably difficult challenges preventing commercial success. In fact, despite significant efforts, only OLEDs have broken into the commercial marketplace with high-profile usage in smart phones and curved displays. For the many other OE devices, performance and reliability remain an enduring challenge. And while each device has had varying

degrees of success in circumventing these problems, the core issue is unlikely to be resolved. As it happens, the same features that make these devices so attractive – *the ultra-thin, lightweight, and flexible architectures* – also makes them notably difficult to control. More specifically, at the heart of these OE devices is a composite arrangement of semiconducting polymers – each specifically tailored to maximize a property or to perform a function (*i.e,* charge conduction or luminescence). It is then the union of these materials, and properties, that gives rise to many multifunctional devices. Then, depending on the nature of the device and the expected functionality, device optimization requires that the two materials be blended (or fabricated) in ways that maximize the intended properties. This notion gives rise to the concept of *structure-sensitive* design and provides the motivation for this work.

While the concept of structure-sensitive design is hardly new, the rapidly increasing power and availability of high-performance computing has provided a new platform for which materials may be studied, designed, and optimized. Further, in light of the immense complexity associated with materials design in semiconducting polymer blends, computational tools are expected become indispensable. Tools ranging from databases and machine learning to modeling, simulation and high-performance computing, will be tightly integrated into the materials design process [13, 14]. It is through this lens that I outline the objectives of this work.

1.1 Objectives

The overarching goal of this research is to explore the process-structure-property relationships governing OE device behavior and to develop extensible computational tools to directly link processing conditions to device performance. This will provide considerable insight towards the rational design of OE devices. More specifically, the objectives are:

i) *Develop predictive modeling capabilities* for a broad class of thin film organic electronic devices. This includes fabrication conditions and material properties for realistic material systems.

ii) *Explore the process-structure-property relationships* governing OE device behavior.

iii) *Develop and employ optimization framework* to automatically link process-to-performance and identify promising processing conditions.

1.2 Overview

This dissertation is organized as follows. Chapter 2 describes the development of a predictive modeling framework for the fabrication of a thin film organic electronic device. In this work, a two-component (binary) polymer blend undergoing thermal annealing with substrate patterning was considered for processing conditions. Then, this morphology evolution framework was integrated with a heuristic optimization scheme to systematically identify promising processing conditions to produce a desired microstructure. Chapter 3 expands on this work by introducing solvent evaporation as a key processing condition. This three-component system (two polymers diluted in a common solvent) provides more realistic fabrication conditions, as most organic electronic devices are produced via solution processing. Here, evaporation rate and substrate patterning wavelength are the tunable processing conditions. Then, since this predictive model is more computationally intensive with a broader solution space, a Bayesian optimization routine is implemented in an effort to identify optimal processing conditions, while minimizing function evaluations. However, instead of focusing on a desired microstructure, this work uses physically meaningful, performance-based morphology descriptors as an objective function – effectively linking the processing conditions with performance. Upon running the optimization routine to maximize performance, the optimal conditions were identified. Finally, Chapter 4 concludes this work by providing a summary of contributions and how these relate to the overall research objectives. Future directions for this research are then discussed, with an eye towards the future of organic electronics as a whole.

CHAPTER 2. AN OPTIMIZATION APPROACH TO IDENTIFY PROCESSING PATHWAYS FOR ACHIEVING TAILORED THIN FILM MORPHOLOGIES

A paper accepted by *Computational Materials Science*

Spencer Pfeifer, Olga Wodo, and Baskar Ganapathysubramanian

Abstract

It is well-known that the performance of thin film organic electronic devices critically depends on the active layer microstructure. Since processing conditions heavily influence the microstructure, identifying optimal fabrication conditions is a crucial step towards the development of high-performance devices. Current state-of-the-art approaches remain predominantly trial-and-error, which are time and resource intensive. In this work, we integrate a morphology evolution framework (based on a phase-field model) with a heuristic optimization scheme to systematically identify promising processing conditions. We show how annealing time and substrate patterning can be simultaneously tuned to achieve a variety of tailored microstructures. The appropriate choice of cost functional is critical to achieving meaningful results. The methodology presented here provides a scalable and extensible approach towards the rational design of tailored microstructures with enhanced functionalities.

2.1 Introduction

Modern engineering applications continue to drive the demand for heterogeneous materials with multi-functional properties [15, 16, 17, 18, 19, 20, 21]. These properties are often dependent on the microstructure and corresponding internal component configurations (atoms, phases, and compounds), which has resulted in a growing emphasis on *microstructure-sensitive design*. The intention is to identify tailored microstructures that exhibit desirable properties; or to determine the processing conditions capable of producing such morphologies. Historically, the design-to-deployment cycle for microstructure-sensitive materials has taken years to even decades to complete. More recently, however, there has been a sustained effort [22, 23, 13] to rapidly accelerate materials development by integrating effective computational tools into the design and development cycle [24, 25]. The rapidly increasing power and availability of high-performance computing has facilitated the development of increasingly sophisticated computational models [13, 14] that permit an exhaustive analysis of the process-microstructure-property relationships. Examples include microstructure-sensitive analysis in metals and multi-component alloys [26, 27, 28, 29], polymer blends [30, 31], and composites [32]. Consequently, such advances have opened up the possibility of coupling these 'forward' models with optimization frameworks to systematically identify promising pathways that produce microstructures with desirable properties [33, 34, 31, 35, 36].

Our focus is on a relatively newer class of microstructure design problems involving polymer blends, in which both anisotropy and confinement play a significant role in determining performance. More specifically, we are interested in the microstructure-sensitive design of polymer-based thin films (or more generally, organic thin films) for use in organic electronics. These devices generally consist of highly anisotropic, multi-component blends, with operational conditions (and hence microstructure design) that must carefully consider the impact of the film boundaries. Applications for such devices range from sustainable energy harvesting and flexible displays [37, 38, 39] to implantable healthcare diagnostic devices and sensors [40, 41, 12]. These devices are particularly attractive because they exhibit an inherent softness, flexibility, and biological compatibility — traits that are traditionally absent in conventional silicon-based systems [41]. In addition, the prospect of an inexpensive, high-speed, 'roll-to-roll' manufacturing process operating at low temperatures, makes organic thin film devices excellent candidates for 'green electronics.'

However, many promising technologies are currently bottlenecked by the manufacturing stage — namely the immense challenges associated with selecting proper fabrication conditions to produce desirable morphologies with tailored properties. Addressing this shortcoming serves as the central motivation for the current work.

In the sections that follow, we focus on developing an extensible and scalable optimization framework that systematically identifies viable processing conditions that result in tailored microstructures. We use the words 'microstructure' and 'morphology' interchangeably. We couple a phase-field-based morphology evolution framework [30, 42, 43] with a particle swarm optimization (PSO) routine. The choice of a meta-heuristic, multi-start, gradient-free optimization routine (in contrast to gradient-based methods) is made to ensure that the phase space is well-explored.

As a representative problem that illustrates this framework, we consider post-deposition annealing of an organic thin film consisting of two distinct materials (*i.e.,* a two-phase system, A-B). Post-deposition annealing (both thermal- and solvent-based) is a routinely used protocol in organic electronics to develop well-connected microstructural domains [44, 45]. The annealing process encourages the progression of spinodal decomposition which is exhibited as coarsening behavior and results in the formation of large (A-rich phase and B-rich phase) domains. The annealing time, thus, affects the resultant final morphology. We choose the annealing time as one of the processing conditions that can be tuned to tailor the morphology. Additionally, we consider the organic thin film to be in contact with a chemically patterned substrate. The localized changes in the surface energy of the substrate (due to the chemical treatment) result in spatial variations in the way that the substrate interacts with the A-rich and B-rich domains within the thin film. Such patterning – in which the chemistry can be tuned to preferentially attract or repel one of the two components – has been shown to be very useful in modulating morphology formation [46], with dip-pen nanolithography being one successfully deployed approach [47, 48, 49, 50]. We choose the patterning wavelength as one of the processing conditions that can be tuned to tailor the morphology. Note that the choice of these two processing variables in our illustrative example of the optimization framework also showcases the interplay between a volume-based control mechanism (annealing) with that of a surface-based control mechanism (substrate patterning). We report results for 2D domains representing the cross-sectional

morphology (i.e. morphology in the direction perpendicular to the plane of the film) as the morphology variation across the depth of the thin film critically affects performance.

The outline of the rest of the paper is as follows: We provide a brief description of the phase-field methodology at the core of our morphology evolution framework in Section 2. Then, Section 3 is devoted to the development of a suitable objective function as well as implementation details of the PSO algorithm — which is developed around two processing conditions: thermal annealing and substrate patterning. Finally, Section 4 provides illustrative results from the optimization framework, followed by concluding remarks in Section 5.

2.2 Morphology evolution & phase-field modeling

In recent years, several groups have utilized phase-field approaches to model morphology evolution in organic thin films [30, 51, 52]. This class of numerical methods has become a staple mesoscale model for simulating interfacial evolution under a wide variety of physical phenomena. Such popularity is a result of the simplicity with which these thermodynamically-driven models are constructed. Moreover, the 'modular' free energy-based design allows for a natural inclusion of diverse physical phenomena as well as material-specific properties — all while supporting short software development cycles [53]. In developing a coupled phase-field–PSO framework, this added versatility allows for an efficient progression from a proof-of-concept model to more realistic systems that incorporate tailoring a broader set of processing conditions (for example, evaporation rates, spinning speeds, temperature ramps, among others).

As previously mentioned, this work explicitly focuses on a two-phase system undergoing thermal annealing in the presence of a chemically patterned substrate. The goal is to design a versatile and robust numerical framework, which is naturally extensible to broader classes of material systems and fabrication techniques.

2.2.1 Phase-field model

The phase-field model defines the evolution of an order parameter, $\phi(\boldsymbol{x}, t) \in [0, 1]$, which represents the local volume fraction of component A (of a binary A-B mixture), with the volume fraction of B given as

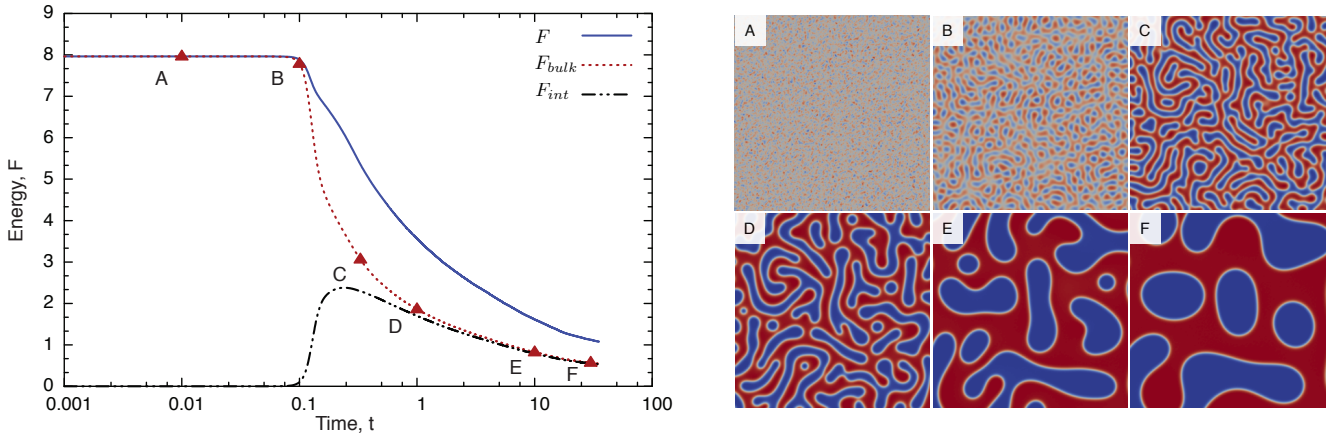

(a) (b)

Figure 2.1: Representative phase-field simulation. (a) Time evolution profiles for the *Total* (F), *Bulk* (F_{bulk}), and *Interfacial* (F_{int}) free energy components (Eqs. 2.1-2.3). (b) Two-dimensional solutions (*top-down*), sampled at several points of interest throughout the evolution.

$1-\phi(\boldsymbol{x},t)$. The evolution equation is derived via formulating (and minimizing) a free energy functional that represents the energy of a given configuration of the system, $\phi(\boldsymbol{x},t)$.

Here, the free energy, F, assumes the typical Ginzburg-Landau form with an added boundary term to include substrate effects:

$$F(\phi) = \int_{\Omega} \Big[f(\phi) + \epsilon^2 |\nabla\phi|^2 \Big] d\Omega + \int_{\Gamma} f_s(\boldsymbol{x},\phi)\, d\Gamma, \tag{2.1}$$

where Ω represents the physical domain, and Γ is limited to the lower boundary of the domain, where the system interacts with the substrate. Here, $f(\phi)$ is the local, *homogeneous* (*bulk*) free energy of mixing, which has a non-convex, double-welled profile for binary systems. For simplicity, this term is often represented by the following quartic polynomial relation:

$$f(\phi) = \frac{1}{4} \cdot \phi^2 (1-\phi)^2. \tag{2.2}$$

The square gradient term in Eq. 2.1 represents the *interfacial* energy, and accounts for the costs associated with interface creation between two immiscible phases. The interfacial coefficient, ε^2, characterizes the interfacial thickness between homogeneous phases and is often correlated with the energy of forming an A-

B interface, which is typically on the order of a few mJ/m^2 for organic blends. Finally, $f_s(\boldsymbol{x}, \phi)$ introduces a spatially-dependent surface potential at the lower boundary to incorporate substrate patterning effects. The total energy can be described as a summation of bulk, interfacial, and surface energy contributions:

$$F = F_{bulk} + F_{int} + F_s, \tag{2.3}$$

which are individually tracked during morphology development, as shown in Figure **??**.

Next, the time evolution of the system is expressed by the following continuity relation:

$$\frac{\partial \phi}{\partial t} = -\nabla \cdot \boldsymbol{J}. \tag{2.4}$$

In which the mass current, $\boldsymbol{J}$, is related to the chemical potential ($\mu = {}^{\delta F}/_{\delta \phi}$), as follows:

$$\boldsymbol{J} = -M \nabla \mu. \tag{2.5}$$

The species mobility, M, is assumed to be spatially uniform and independent of concentration (we set $M = 1$). Combining the above, we arrive at the Cahn-Hilliard (CH) equation:

$$\frac{\partial \phi}{\partial t} = \nabla \cdot \left[M \nabla \left(\frac{\partial f}{\partial \phi} - \varepsilon^2 \nabla^2 \phi \right) \right]. \tag{2.6}$$

Characteristic solutions, absent of substrate effects, are provided in Figure **??** above. Here, images (A)-(F) provide representative snapshots throughout the morphology evolution – each corresponding to a significant point along the bulk energy profile, F_{bulk}, in Figure **??** (a). More specifically, points (A) and (B) represent a disordered phase prior to bulk segregation. The short moments thereafter are characterized by a significant plunge in the bulk energy before arriving at point (C). This rapid energy dissipation, characteristic of phase separating systems, coincides with a maximum in the interfacial energy component (F_{int}). In the course of minimizing the total free energy (F), component-rich domains rapidly emerge forcing the creation of interfacial boundaries. Then, as the system continues to evolve towards an equilibrium concentration, interfaces slowly diminish, and component-rich domains coarsen – resulting in further energy dissipation, now at a much slower rate. This *coarsening* phase, reflected in points (D), (E), and (F), represents approximately 20%, 10%, and 7% remaining bulk energy, respectively. This coarsening stage, characterized by consistent domain growth, has been shown to model thermal annealing.

2.2.2 Substrate patterning

Since thin films are often characterized by large surface-to-volume ratios, the presence of a boundary is known to play a significant role in the microstructure development process (due to confinement, surface chemistry, and surface roughness, to name a few). Chemically patterning the substrate, via dip-pen nanolithography or microcontact printing, has proven to be an effective means of influencing the thin film morphology [47, 48, 49, 50]. We now define an additional surface energy component, F_s, designed to selectively introduce the effects of substrate patterning as a means of influencing the bulk morphology throughout the annealing process. This is introduced through the following surface integral:

$$F_s(\boldsymbol{x}, \phi) = -\int_\Gamma f_s(\boldsymbol{x}, \phi)\, d\Gamma, \tag{2.7}$$

$$= -\int_\Gamma p(\boldsymbol{x})(h\phi + \frac{1}{2}g\phi^2)\, d\Gamma. \tag{2.8}$$

Here, the spatially-dependent function, $p(\boldsymbol{x}) \rightarrow \{\text{-}1, 0, 1\}$, describes the local, point-wise, nature of the surface pattern. A non-zero value, $p(\boldsymbol{x}) = \pm 1$, at point $\boldsymbol{x}$, indicates an *attractive* or *repulsive* surface chemistry towards one component. Otherwise, a zero-value is imposed, indicating component neutrality. The magnitude of the surface potential is then introduced through the parameters h and g [54, 55].

Throughout this work, homogeneous Neumann boundary conditions are imposed at the upper boundary for ϕ and μ, $\{\hat{\boldsymbol{n}} \cdot \boldsymbol{\nabla}\mu = 0$ and $\hat{\boldsymbol{n}} \cdot \boldsymbol{\nabla}\phi = 0\}$, while homogeneous Neumann boundary conditions are applied for μ at the lower boundary. However, at the lower surface ($y = 0$), substrate effects are introduced as non-zero, local equilibrium values for ϕ as:

$$\hat{\boldsymbol{n}} \cdot \boldsymbol{\nabla}\phi = h + g\phi. \tag{2.9}$$

This formulation is based on the assumption that the surface free energy reaches an equilibrium well before that of the bulk, thereby satisfying these conditions [56, 57, 58]. Periodic conditions are enforced laterally on the size wall boundaries.

2.2.3 Numerical implementation

The Cahn-Hilliard equation is solved via continuous Galerkin (CG) finite elements, coupled with an order-adaptive, implicit Runge-Kutta (RK) time scheme [30, 42]. In the present work, simulations are

performed on two-dimensional cross-sections, with each dataset consisting of 600×60 linear elements. This $10 : 1$ aspect ratio provides a rich set of structural features while requiring modest computational resources.

Several key parameters that characterize the system's behavior are next set. In light of our intended application, we select a simplified 'model' system, in which all parameters exist in dimensionless form. We set the interfacial coefficient to be $\epsilon^2 = 6\text{E-}5$ and consider an off-critical blend ratio of $\phi_0 = 0.5238$ $(1 : 1.1)$. Then, to initiate phase separation and ensure reproducibility, each simulation is initialized with an *identical* Gaussian-distributed random field: $\phi(\boldsymbol{x}, 0) = \phi_0 + \mathcal{N}(0, \sigma)$, in which $\sigma = 0.005$.

The substrate patterning scheme consists of an alternating attractive/repulsive motif applied to the lower boundary. In this work, the function, $p(\boldsymbol{x})$, is taken to be a square wave of the form:

$$p(\boldsymbol{x}) = \text{sign}(\ \sin(2\pi \cdot \boldsymbol{x}/\lambda_p)\ ), \tag{2.10}$$

in which $\text{sign}(x)$ refers to the sign (signum) function:

$$\text{sign}(x) = \begin{cases} 1 & \text{if } x > 0 \\ 0 & \text{if } x = 0 \\ \text{-1} & \text{if } x < 0 \end{cases} \tag{2.11}$$

and λ_p is the patterning wavelength. Several variants of this formula have been implemented by others to achieve similar effects [56, 59]. The surface potential coefficients, h and g in Eq. 2.8, are set to: $h = 5\text{E-}4$ and $g = 0$. These values, chosen heuristically, were selected to maximize the surface influence.

Finally, the nonlinear system is solved using an in-house, finite element (FEM) framework written in C++, which utilizes a parallelized Newton-Raphson scheme provided by the PETSc solver library [60]. Figure 3.1 provides illustrative datasets (truncated for visualization purposes), over a range of surface patterns.

2.3 Optimization

We next formulate the problem of identifying the fabrication conditions (namely, substrate patterning wavelength and annealing time) that result in desirable morphologies as an optimization problem. To do so,

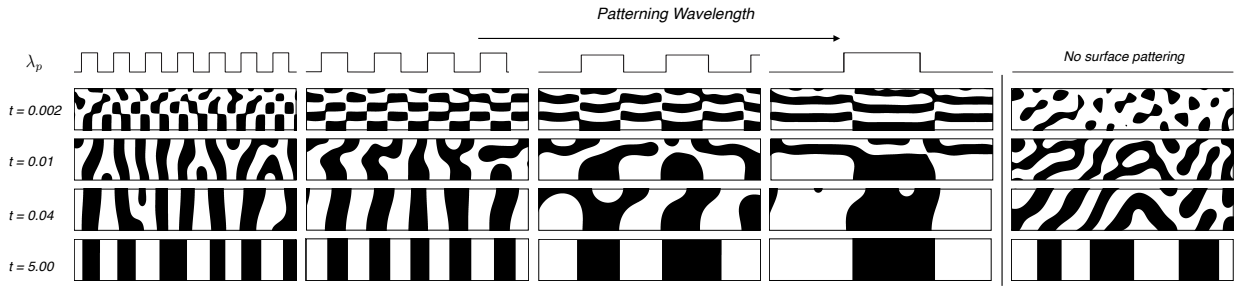

Figure 2.2: Illustrative representations of microstructural evolution on a patterned substrates (*images have been truncated for visualization purposes*). Full simulations are performed on 600×60 element 2D cross sections (with only one-fourth of the domain, 150×60 shown), with $\phi_0 = 0.5238$, $\epsilon^2 = 6\text{E-}5$, and surface pattern, λ_p, applied at lower boundary, with surface potential, $h = 5\text{E-}4$.

we seek to minimize an objective function $\mathcal{F} : A \rightarrow \mathbb{R}^+$, given a desired *target* morphology. The task of the objective function is to encode deviations of an arbitrary morphology (due to processing conditions A) from that of the target. Thus, the objective function maps the space of processing conditions (our search space) to a positive real number (with larger numbers indicating larger deviation from the desired morphology).

Designing an effective objective function is exceedingly application-dependent and often non-trivial, as it requires certain prior knowledge about the solution space. In our particular case, the objective function should compare key morphological features, while maintaining translation invariance (as shifted morphologies perform identically). This function should also penalize large-scale morphological deviations from the target while remaining insensitive to minor variations. Finally, a reasonably 'smooth' objective function is highly sought after, as this allows for a more efficient solution convergence. To meet these requirements, no single metric was considered. Rather, the careful design of the objective function resulted in the inclusion of several functions that targeted each of the above requirements.

2.3.1 Objective function

Given a target $\tilde{\phi}$, and candidate microstructure, ϕ, the objective function, $\mathcal{F}(\phi, \tilde{\phi})$, is a measure of the relative 'fitness' of the candidate and is often quantified by a mean-squared-error (MSE) [31, 61]. This popular approach has the benefit of mathematical simplicity with minimal overhead; and in many cases, provides

reliable convergence. However, for more complex datasets, such as those shown in Figure 3.1 (and other random heterogeneous microstructures [62]), point-wise measures alone often return mixed results, due to the fact that such measures are insensitive to translation, rotation, or scale variations. Point-wise evaluations are most successful when the target and candidate solutions are structurally similar; otherwise such methods often produce a highly corrugated function space. Thus, it is important to incorporate statistical measures of the morphology as well. For instance, in many thin-film applications, the general structure, average domain size, and connectivity are of primary interest, among others [63].

In addition to traditional point-wise metrics, we have assembled a set of microstructure-sensitive morphology descriptors to extract specific features of interest. A linear combination of each descriptor, in conjunction with heuristic penalty functions, provides a clear contrast between different morphologies, while maintaining a reasonably smooth search space topology. The metrics employed in this work are: the $\mathcal{L}_2$-*norm*, the *structural similarity index* (SSIM), and the *characteristic length scale*; each of which are now discussed.

2.3.1.1 Relative $\mathcal{L}_2$-Norm

First, we utilize the simplest measure for evaluating the point-wise error between two morphologies, which is the $\mathcal{L}_2$-norm. For a vector, $\boldsymbol{y} \in \mathbb{R}^n$, the $\mathcal{L}_2$-norm is defined $\|\boldsymbol{y}\|_2 \equiv \left(\sum_{i=1}^{n} y_i^2\right)^{1/2}$. The relative error between the target, $\tilde{\phi}$, and candidate, ϕ, morphologies, is described by:

$$\sigma_{\mathcal{L}_2} = \frac{\|\tilde{\phi} - \phi\|_2}{\|\tilde{\phi}\|_2}. \tag{2.12}$$

This metric is very useful in assessing the difference between two morphologies of relatively similar features and topology. However, the inherent point-wise differencing makes this metric sensitive to geometric differences (scaling, translation). This may introduce disproportionate variations in the cost function landscape, which can critically affect the solution efficiency and accuracy.

2.3.1.2 Structural similarity index

To counter these shortcomings, we now turn towards a 'perception-based' methodology to evaluate the *structural similarity* (SSIM) between morphologies. This index was proposed by Wang *et al.* [64], in an ef-

fort to imitate characteristics of the human visual system, which is highly adapted for recognizing structural information. Often described as a 'top-down' approach, the SSIM index identifies and compares patterns and correlations, within a local window. This 'structural' paradigm is a very popular image processing technique, routinely used in transmission, compression, and restoration algorithms [65, 66]. The SSIM index is defined as a product of comparisons for three image characteristics: the *luminance*, *contrast*, and a combination of correlation distortions, collectively designated as the *structural* component. The overall similarity measure is given as:

$$S(\boldsymbol{x}, \boldsymbol{y}) = [l(\boldsymbol{x}, \boldsymbol{y})]^{\alpha} \cdot [c(\boldsymbol{x}, \boldsymbol{y})]^{\beta} \cdot [s(\boldsymbol{x}, \boldsymbol{y})]^{\gamma}. \tag{2.13}$$

In which,

$$l(\boldsymbol{x}, \boldsymbol{y}) = \frac{2\mu_x\mu_y + c_1}{\mu_x^2 + \mu_y^2 + c_1}, \quad c(\boldsymbol{x}, \boldsymbol{y}) = \frac{2\sigma_x\sigma_y + c_2}{\sigma_x^2 + \sigma_y^2 + c_2}, \quad s(\boldsymbol{x}, \boldsymbol{y}) = \frac{\sigma_{xy} + c_3}{\sigma_x\sigma_y + c_3}, \tag{2.14}$$

define the luminance, contrast, and structural terms, respectively. Here, μ_x and μ_y are the sample means, σ_x^2, σ_y^2, are the variances, and σ_{xy} is the sample cross-correlation between datasets ($\boldsymbol{x}$, $\boldsymbol{y}$). The exponential weighting parameters, α, β, and γ may be used to emphasize various components, but are often unity by default, $\alpha = \beta = \gamma = 1$. The constants, c_1, c_2, c_3 are small values included to avoid instabilities and are often length-scale dependent. Following standard practice, we set $c_3 = c_2/2$, in which case the similarity index simplifies to:

$$S(\boldsymbol{x}, \boldsymbol{y}) = \frac{(2\mu_x\mu_y + c_1)(2\sigma_{xy} + c_2)}{(\mu_x^2 + \mu_y^2 + c_1)(\sigma_x^2 + \sigma_y^2 + c_2)}. \tag{2.15}$$

The SSIM index provides several appealing properties, including symmetry ($S(\boldsymbol{x}, \boldsymbol{y}) = S(\boldsymbol{y}, \boldsymbol{x})$), boundedness ($S(\boldsymbol{x}, \boldsymbol{y}) \leq 1$), and a unique maximum; that is, $S(\boldsymbol{x}, \boldsymbol{y}) = 1$, if and only if $\boldsymbol{x} = \boldsymbol{y}$. As part of our objective function, we define:

$$\sigma_{SSIM} = 1 - S(\boldsymbol{x}, \boldsymbol{y}), \tag{2.16}$$

which quantifies the relative dissimilarity between datasets. Note that σ_{SSIM} tends towards zero when $\boldsymbol{x} \to \boldsymbol{y}$.

2.3.1.3 Characteristic length scale, R_g

To further discriminate between morphological features we consider the characteristic length scale, R_g. In regards to microstructural characterization, this metric has been widely used to study the growth kinetics in spinodal decomposition [67, 68], as it effectively captures the average domain size of the morphology. For this work, the characteristic length scale is extracted from the equal-time pair correlation [62, 69]:

$$C(\boldsymbol{r}, t) = \langle \phi(\boldsymbol{x} + \boldsymbol{r}, t)\phi(\boldsymbol{x}, t) \rangle \,, \tag{2.17}$$

in which the first minimum (of the normalized pair correlation) is denoted as R_g and integrated into the objective function as follows:

$$\sigma_{R_g} = \frac{\left| \tilde{R}_g - R_g \right|}{\tilde{R}_g}, \tag{2.18}$$

where $\tilde{R}_g$ is the characteristic length scale of the desired microstructure.

2.3.1.4 Penalty functions

Next, due to the inherent diversity of possible morphologies produced by the phase-field framework, heuristic information is included through the use of two penalty functions. The first, P_{cc}, places a *deadzone-linear* penalty on the number of connected components, η_{cc}, within the morphology[1]. For thin morphologies, this amounts to the number of domains and effectively discards *undeveloped* (*or checkered*) morphologies (Figure 3.2 provides representative examples of four notable structures). This penalty is implemented as follows:

$$d_{cc} = \left| 1 - \frac{\eta_{cc}}{\tilde{\eta}_{cc}} \right|, \tag{2.19a}$$

$$P_{cc} = 1 + \max(0, d_{cc} - a_1). \tag{2.19b}$$

Here, $\tilde{\eta}_{cc}$ defines the number of target connected components (computed from the desired morphology, $\tilde{\phi}$), with a_1 as a heuristic barrier limit. Next, since we are primarily interested in *columnar* microstructures,

[1] Connected components are computed in `MATLAB` using the Image Processing Toolbox [70].

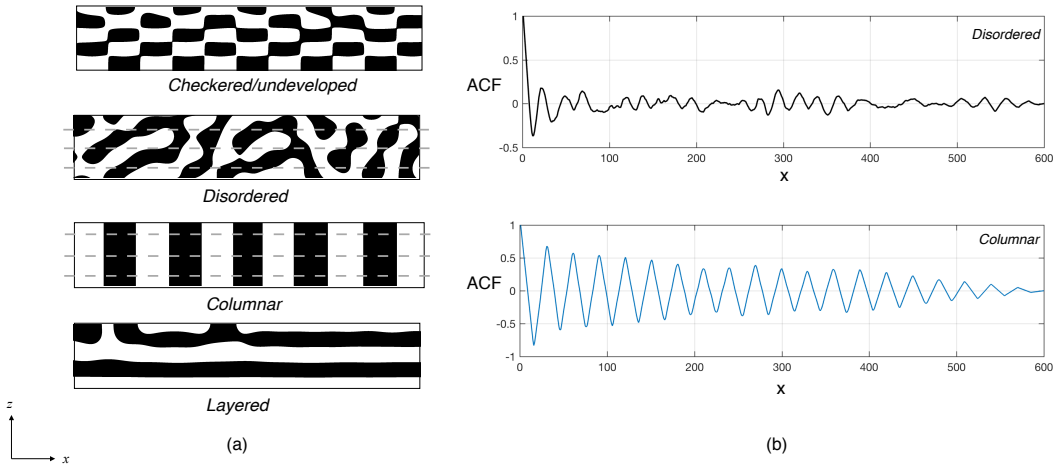

Figure 2.3: (a) Illustrative representations of four typical morphologies. The *checkered* structure is induced by the substrate pattern and appears immediately after phase separation. *Disordered* and *columnar* structures appear at the later-stages and depend on the efficacy of the substrate pattern. The *layered* structure is generally present for homogeneously patterned surfaces (all attractive or all repulsive). (b) 1D autocorrelation (ACF), averaged over the three slices shown, for the *disordered* and *columnar* structures to the left. The ACF is used as a penalty function to differentiate between structures.

we impose a second penalty function that is specifically tailored to favor microstructures of this type (see Figure 3.2). A clear distinguishing feature of the columnar microstructure, is the uniformity in the *z-dir*; hence, we now impose a penalty for structures with high variations in the vertical columns (non-columnar). This is implemented by computing the 1D autocorrelation for several slices in the *z-dir*. A *log-barrier* penalty, is then imposed for structures with large deviations:

$$P_v = \begin{cases} -\log(1 - d_v/a_2), & \text{if } d_v < a_2, \\ 2.0 & \textit{otherwise}, \end{cases} \tag{2.20}$$

in which d_v is defined as the relative error between the target and candidate autocorrelations described above ($\tilde{C}_y$ and C_y, respectively):

$$d_v = \frac{\|\tilde{C}_y - C_y\|_2}{\|\tilde{C}_y\|_2}. \tag{2.21}$$

Here, a_2 is a relative tolerance $a_2 = 1 + \epsilon$ (here we have selected $\epsilon = 1\text{E}^{-2}$). This simple formulation effectively penalizes non-uniformity in the *z-dir* as well as large deviations from the target. While other cost function components are naturally extended to more general problems, this heuristic penalty is only applicable for columnar microstructures, since we take advantage of a unique structural feature. However, this provides an example of tailoring the objective function for specific applications, which may be critical to the success of the algorithm.

Remark. A linear combination strategy is employed to combine the above measures into a single scalar objective function, representing the relative similarity, or error, between the computed and desired morphologies:

$$\mathcal{F}(\phi, \tilde{\phi}) = \left[\sum_{i=1}^{3} w_i \cdot \sigma_i \right] \cdot \frac{\max\left(P_{cc}, P_v\right)}{\sum w_i}. \tag{2.22}$$

Our objective function now consists of four primary parts: a *statistical* measure, an *image processing* measure, and a *microstructural descriptor*, moderated by structure-selective, *penalty functions*. As a means for tuning the multi-component objective function, each component is weighted by a factor $w_i = [1.0, 1.25, 2.0]$, before the larger of the two penalty functions is applied; as described by Kulkarni *et al.* [71].

It should be noted that several other characterization metrics were considered. However, we discovered that this combination of measures provided the most consistent results and sufficiently encompassed the diversity of microstructural variability presented by this problem. Alternative measures, including: statistical moments [72], image entropy, energy-based metrics, homological descriptors (such as the Euler characteristic and Betti number) [68, 73], graph-based approaches [63], additional correlation formulations [62], as well as more advanced SSIM measures [74], were all considered.

2.3.2 Particle swarm

We choose to utilize metaheuristic optimization routines, as derivative information is unavailable and multiple local optima are anticipated. While numerous metaheuristic methods are available (*Genetic Algorithms (GA), Particle Swarm (PSO), Simulated Annealing (SA), Ant Colony Optimization (ACO)* and several more [75, 76]), we chose a standard PSO algorithm. This scheme offers simplicity and flexibility with a minimal computational overhead. In addition, numerous software packages, written in high-level languages (*i.e.,* `MATLAB`, Python) are available, which provides an ideal development environment.

Developed by Eberhart and Kennedy in the mid-90's, PSO is often associated with bird flocks or similar patterns of 'swarm' movements — as these social behaviors gave rise to its conception [77]. This paradigm has since evolved and expanded to numerous fields of study; and while more sophisticated algorithms have been developed, PSO remains extremely popular — largely due to the simplicity, robustness, and generally high performance for a broad spectrum of applications [78, 79].

In its simplest form, PSO is a collection of particles dispersed across the entire parameter space, in search of a global minimum. Each particle, or candidate solution, is given an initial position and velocity and is allowed to move about the space, evaluating its fitness at each step. However, in analogy to the swarm behaviors observed in nature, each particle communicates fitness information with other members of the swarm. Consequently, each succeeding movement is partially influenced by the best-known global position and that of the individual particle's best-known position. As a result, each particle is able to avoid local minima and migrate towards a global solution [78, 80].

Mathematically, the velocity vector for each particle, $\boldsymbol{v}_i^{n+1}$, is generally defined as follows:

$$\boldsymbol{v}_i^{n+1} = \alpha \boldsymbol{v}_i^n + c_1 r_1 (\hat{\boldsymbol{x}}_\ell^\star - \boldsymbol{x}_i^n) + c_2 r_2 (\hat{\boldsymbol{x}}_g^\star - \boldsymbol{x}_i^n). \tag{2.23}$$

This relationship is often described as a combination of *inertial*, *local*, and *global* terms, with α, c_1, c_2 as tunable parameters[2]. Here, $\hat{\boldsymbol{x}}_\ell^\star$ and $\hat{\boldsymbol{x}}_g^\star$, represent the *best-known* candidate solutions for the individual particle and all particles, respectively. The values $r_1 \in (0, 1)$ and $r_2 \in (0, 1)$ are uniform random numbers, regenerated at each iteration. Next, each particle position is updated as follows:

$$\boldsymbol{x}_i^{n+1} = \boldsymbol{x}_i^n + \boldsymbol{v}_i^{n+1}. \tag{2.24}$$

At each position, the objective function, $\mathcal{F}$, is evaluated and communicated globally. The algorithm continues iterating until a tolerance requirement has been achieved [78, 79].

2.3.3 Implementation

The PSO algorithm is summarized in Figure 2.4; the core functionality of which is derived from the built-in `MATLAB`$^{\text{TM}}$ PSO package. After spawning an initial population, this function makes calls to the phase-field-based morphology simulator, described in Section 2, and evaluates the objective function for each particle, as described in Eq. 2.22. For this application, we employ a *two-stage* PSO algorithm. The first execution casts a broad range of particle positions, spanning the entire search space. This stage is only allowed to run for a fixed number of iterations before exiting. The second execution, acting as a refinement step, spawns a reduced number of particles spanning a subspace region identified in the first stage, and iterating until a tolerance condition is met. This hierarchical approach allows for a more rapid convergence, as the function evaluations are computationally expensive.

The two processing conditions of interest to be optimized, thermal annealing and substrate patterning, are represented by time, t, and patterning wavelength, λ_p, respectively. For each particle, whose position represents a specific (t, λ_p), we run the morphology evolution with the specified patterning wavelength from $t = 0$ until late-stage (*i.e.* morphology features do not change with time), and evaluate the objective function at the specified time. This also allows us to store the intermediate morphologies and to evaluate the objective function at these intermediate time steps.

[2] *Typical values for each term:* $(0 \leq \alpha \leq 1.2)$, $(0 \leq c_1/c_2 \leq 2)$

2.4 Results

We choose our desired morphology to be one with alternating columns of donor-rich and acceptor-rich domains (see Figure 2.5 (bottom)). Our interest in identifying conditions that may produce this morphology stems from applications in organic electronics, specifically organic photovoltaics [81, 82]. It is generally accepted that morphologies with alternating columns of donor-rich and acceptor-rich domains (a variant of the so-called 'saw-tooth' morphology) make optimal photovoltaic devices [83, 84, 85, 86, 87, 88, 81, 82]. This morphology consists of domains whose characteristic length scales enable a large fraction of the excitons to diffuse towards the donor-acceptor interface, a large donor-acceptor interfacial area allows efficient exciton dissociation, as well as straight pathways that facilitate charge transport with minimal recombination [89]. This intuition has been backed by various numerical investigations [90, 91, 92, 93, 94, 95].

As mentioned above, the intrinsic length scale of the material system has strong implications for device properties and is often a critical quantity of interest in material selection and fabrication. This dominant length scale of the system is defined by the characteristic domain size of the morphology at the onset of phase separation (assuming no substrate patterning or other forces are present). However, substrate patterning has been shown to be effective for patterns *commensurate* with the intrinsic domain size, which we call λ_d [96]. More specifically, it has been shown that the best pattern replication (or morphology control) is attained when the lengths scales of the substrate pattern and material system are commensurate; that is, $\lambda_p/\lambda_d \approx 1$. We therefore normalize our length scales in terms of this length scale, λ_d. This normalization in terms of the characteristic scales of the material system enable broader applicability of these results to other material systems.

Next, we consider three distinct columnar morphologies (*morphology 1, 2 and 3*), each with varying column widths. Morphology 1 has column width equivalent to the intrinsic domain size, while morphologies 2 and 3 are defined to be $2\lambda_d$ and $\lambda_d/2$, respectively. In the context of our application, we seek to investigate the possibility of tuning the column spacing, in order to maximize the exciton dissociation capability under varying charge mobility conditions [42]. This will provide a rational approach in selecting fabrication conditions to guide the morphology evolution towards distinct structures of interest, exhibiting high internal quantum efficiencies. It is important to note that the solution space of accessible morphologies is rather di-

verse with several distinct morphology classes, including *columnar, undeveloped, disordered, and lamellar*. Figs. 3.1 & 3.2 provide several representative morphologies, rendered at selected points of the two design variables — patterning wavelength and annealing time.

Fabrication conditions for Morphology 1: The first columnar morphology we choose has a characteristic columnar thickness of λ_d, as shown in Figure 2.5 (bottom). The objective function is shown in Figure 2.5 (top) and is constructed by sampling across the range of the accessible search space. Several representative images at selected points are also provided, indicating not only the interconnected structure, but also columnar structures with spatially-varying widths. This figure not only provides a clear representation of the design landscape but also reveals a unique perspective into the competition between bulk phase separation and substrate patterning. A prominent feature of this surface plot is the *ridge-line*, at approximately $t = 0.5$. This is the transition point from a disordered phase into a columnar phase, which is specifically captured by the penalty functions. Cutting through the middle is the narrow subspace in which the desired morphology may potentially exist. Not surprisingly, this region corresponds to a *commensurate* pattern, in which the characteristic length scale of the substrate pattern is similar to the characteristic length scale of the domain, $\lambda_p/\lambda_d \approx 1$. As a result, good pattern replication is observed immediately after phase separation, followed by very limited domain growth throughout the simulation. However, just outside of this narrow parametric region, defects begin to arise in the pattern replication as domains are stretched beyond what is energetically favorable. This instability leads to large clusters in isolated regions of the microstructure and steep gradients in the objective function. The results from performing the PSO optimization are shown in Figure 2.5 (bottom) (labeled as ϕ_{opt}). As would be expected, the case of commensurate patterning was found with relative ease. The total number of function evaluations was 90 (with half in the first stage and half in the second). The total time for the optimization was approximately 6 hours on a multi-core (12) machine. The produced optimal morphology has a final cost functional value of 0.15. This non-zero evaluation may be attributed to the notable defect found in a few columns of ϕ_{opt} as seen in Figure 2.5 (bottom).

Fabrication conditions for Morphology 2: We next consider a columnar morphology with a larger domain width than the characteristic length scale of the system (the desired width is twice the intrinsic width). Here the patterning wavelength that we expect will be non-commensurate to the intrinsic pattern

formation in the domain. Again, in this context, it was very informative to plot the cost functional across the accessible range of design parameter variations, which is shown in Figure 2.6 (top). The mismatch between the desired length scale and intrinsic length scale produces a pronounced competition between the bulk and surface forces. While a small channel through the region of the target solution, $\lambda_p/\lambda_d = 0.5$, is visible, it is notably less pronounced than the previous case. Notice that at early stages of the annealing the substrate presence maintains a relatively strong influence, as is made clear by the notable depression at the far end of the channel. Throughout the later stages of the evolution, in which domain sizes are relatively large, the microstructures are notably less sensitive to patterning changes; and, by extension, defects — as the larger gaps prevent propagation. Hence, the pattern replication is relatively high while remaining insensitive to various instabilities. We hypothesize that this may hold for additional forcing terms as well (*i.e.,* thermal noise, changes in initial conditions). The results from performing the PSO optimization are shown in Figure 2.6 (bottom) (labeled as ϕ_{opt}). While the columnar widths are slightly larger than those of the desired morphology, the overall result is quite close to the desired morphology. Similar to the earlier case, the complete optimization required about 90 function evaluations, taking approximately 5 hours of compute time.

Fabrication conditions for Morphology 3: We next consider a columnar morphology with a smaller domain width than the characteristic width of the system (desired width is half the intrinsic width). We note that this is a much tougher problem to solve than the previous two cases. This is due to the fact that (a) we seek to freeze the structure at a length scale that is much smaller that the intrinsic length scale, and (b) one of the design variables, annealing time, effectively tries to make the domains larger. Figure 2.7 (top) plots the objective function landscape for this case. This landscape is quite different from the previous two cases with no clearly defined region of pattern replication. Instead, the ridge-line opens up into a broad valley, over which multiple candidate 'best' solutions exist. Within this region, the domain structures are well contained, and a columnar pattern is produced, but the objective function value remains relatively high. This is due to the fact that the domain structures are highly irregular and rarely form straight columns with consistent spacing. However, on average, the domain sizes are nearly half the size of the inherent length scale. We note that multiple (sub) optimal solutions exist. Computationally, the complete optimization required nearly 110

functional evaluations and took nearly 12 hours to identify one of the solutions. Figure 2.7 (bottom) shows the identified morphology.

2.5 Conclusions

In this work, we deployed an integrated process-structure exploration framework for automated identification of promising fabrication conditions to produce a desired morphology. We formulated the exploration process as an optimization problem. We emphasize that crafting an appropriate cost functional is critical to producing effective results. In this work, we utilized a standard particle swarm optimization scheme to optimize a cost functional depending on two fabrication parameters (annealing time and patterning wavelength). We illustrated this framework by identifying conditions that would result in columnar morphologies with three distinct length scales. This framework opens up the possibility of an efficient, automated, and rational identification of processing conditions to produce tailored morphologies.

Future work will focus on expanding this methodology for efficient deployment on large computing clusters. This will enable the optimization of considerably more complex material systems and processing conditions. A natural next step would also be to consider the solvent fabrication process, where there are more variables that can be controlled (solvent type, and solvent evaporation rate). This will provide a more comprehensive approach to designing tailored microstructures.

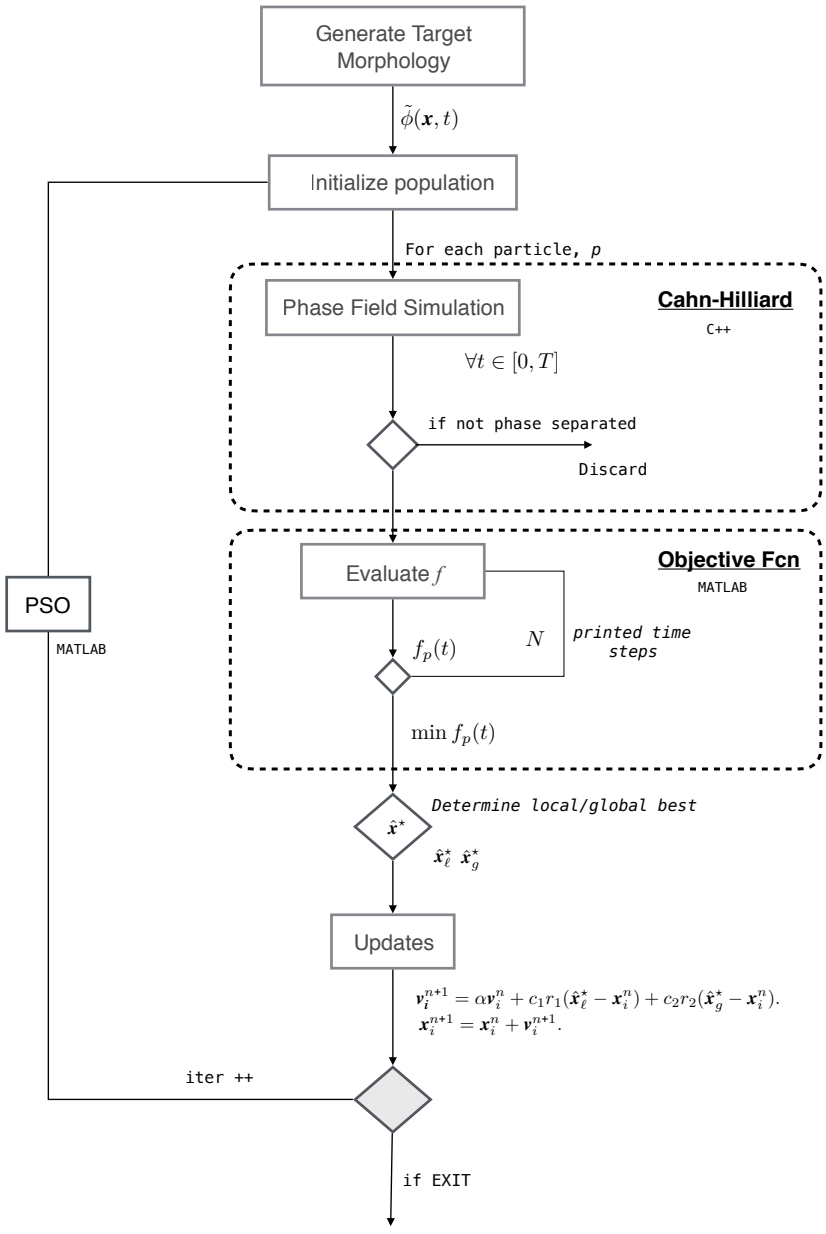

Figure 2.4: Particle Swarm Optimization (PSO) methodology.

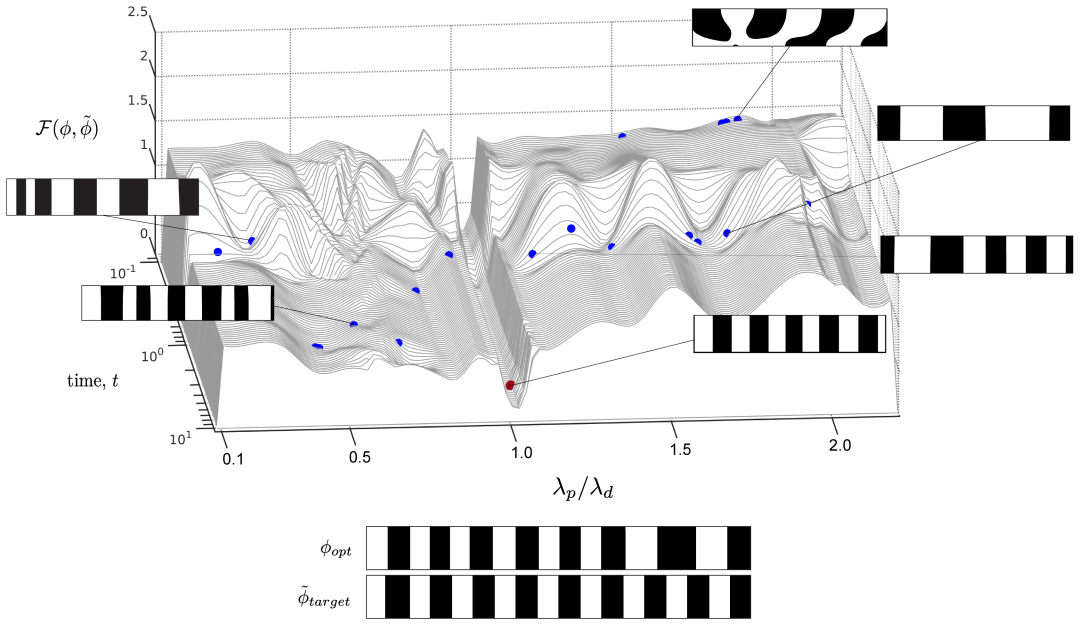

Figure 2.5: (Top) The objective function evaluated across the search space. Blue points indicate the initial particle swarm positions ($N = 20$), while the red point indicates the final convergent position. (Bottom) The desired morphology, labeled $\tilde{\phi}_{target}$, and final identified morphology, labeled ϕ_{opt}. Images have been truncated for visualization purposes. The images in the insets are one-fourth of domain while the two images at the bottom show one-half of domain.

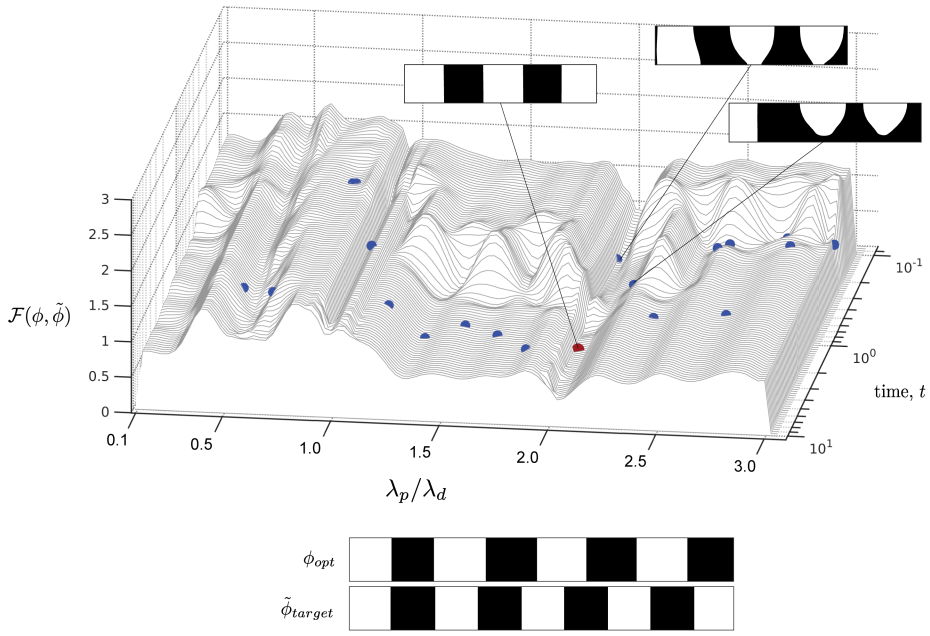

Figure 2.6: (Top) The objective function evaluated across the search space. Blue points indicate the initial swarm positions ($N = 20$), while the red point indicates the final convergent position. (Bottom) The desired morphology, labeled $\tilde{\phi}_{target}$, and final identified morphology, labeled ϕ_{opt}. Images have been truncated for visualization purposes. The images in the insets are one-fourth of domain while the two images at the bottom show one-half of domain.

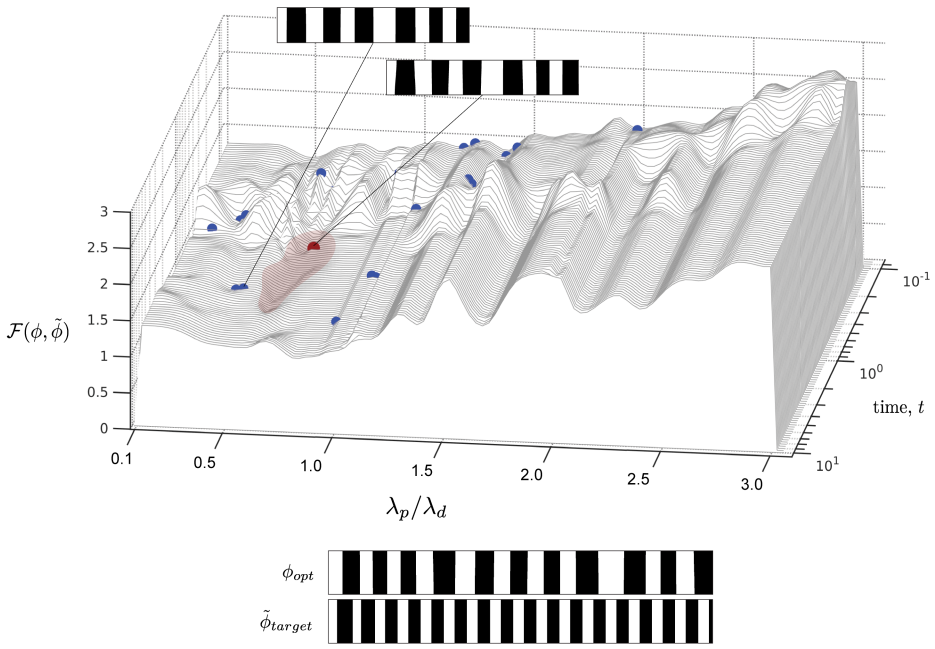

Figure 2.7: (Top) The objective function evaluated across the search space. Blue points indicate the initial swarm positions ($N = 20$), while the red point indicates the final convergent position. (Bottom) The desired morphology, labeled $\tilde{\phi}_{target}$, and final identified morphology, labeled ϕ_{opt}. Images have been truncated for visualization purposes. The images in the insets are one-fourth of domain while the two images at the bottom show one-half of domain.

CHAPTER 3. PROCESS OPTIMIZATION FOR MICROSTRUCTURE-DEPENDENT PROPERTY MAXIMIZATION IN THIN FILM ORGANIC ELECTRONICS

A paper submitted for publication in the journal *"Materials Discovery"*

Spencer Pfeifer, Balaji Sesha Sarath Pokuri, Pengfei Du, and Baskar Ganapathysubramanian

Abstract

The processing conditions during solvent-based fabrication of thin film organic electronics significantly determines the ensuing microstructure. The microstructure, in turn, is one of the key determinants of device performance. In recent years, one of the foci in organic electronics has been to identify processing conditions that result in devices with enhanced properties. This has traditionally involved cumbersome trial-and-error exploration, or a parametric sweep of a large space of processing conditions, both of which are time and resource intensive. This is especially the case when the process → structure and structure → property simulators are computationally expensive to evaluate, thus precluding an exhaustive parametric search.

In this work, we integrate an adaptive-sampling based gradient-free optimization strategy – Bayesian optimization – with a phase-field based morphology evolution framework that models solvent-based fabrication of thin film polymer blends (process → structure simulator) and a graph-based morphology characterization framework that evaluates the photovoltaic performance of a given morphology (structure → property simulator). We illustrate this framework by identifying two processing parameters, the solvent evaporation rate and the substrate patterning wavelength, in a model system that results in a device with enhanced photovoltaic performance evaluated as the short-circuit current of the device.

The Bayesian-based optimization approach adaptively adjusts the two processing parameters to rapidly identify the best processing configuration, thus substantially reducing the computational effort in this process → structure → property exploration. We illustrate how changing the material properties of the model system result in distinctly different optimal processing conditions that enhance performance. The method-

ology presented here provides a scalable and extensible approach towards the rational design of tailored microstructures with enhanced functionalities.

3.1 Introduction

The field of organic electronics continues to grow at a rapid pace, delivering a number of emerging technologies with disruptive potential [97, 6, 98, 1, 99]. This includes organic photovoltaics (OPVs) [100, 99], light-emitting diodes (OLEDs) [1, 101], transistors (OFETs) [9, 8], memory diodes [102, 103], and energy storage devices [104], to name a few. Such broad appeal stems from the unique properties attributed to the semiconducting polymers/small molecules at the heart of organic electronic devices; namely, the familiar electronic functionality, packed into an ultra-thin, lightweight, yet flexible form factor [1]. Moreover, such devices may be sustainably produced at low-costs through established high-throughput printing processes [3, 4]. With the increasing availability of biodegradable and nontoxic organic materials, these scalable printing techniques are expected to pave the way for disposable designs with minimal environmental impact - marking a significant step towards a fully-sustainable product development pipeline [2].

However, despite significant progress over the years, relatively few applications have attained market-ready status. In many cases, performance improvement and long term reliability remain challenges. A common denominator to these challenges is often understanding and controlling the (active layer) microstructure, which is known to critically affect the overall device performance [100, 105, 102, 106]. More specifically, there remains a limited understanding as to how fabrication processes influence morphology evolution, and subsequently how this morphology affects the device performance. This link is often described as a *process–structure–property* (PSP) relationship; a comprehensive understanding of which would provide a recipe for fabricating devices with designer properties. Numerous emerging areas, such as wearable electronics, RFID tags (a key component for the Internet of Things (IoT) paradigm [5]), and bioelectronics [6, 7, 8], would significantly benefit from an improved understanding of the underlying PSP relationships. Consequentially, as part of a community-wide effort to shed more light on PSP relationships and accelerate materials development, a concerted effort has been directed towards high-throughput methodologies and intelligent database mining, as well as the development of increasingly sophisticated

computational models [14, 107, 31, 108, 109, 110]. It is this latter point that provides the inspiration for this work. The development of extensible and highly efficient 'forward' models allows for established optimization frameworks to systematically identify promising pathways that produce microstructures with desirable properties [33, 34, 31, 35, 36].

In our previous work [111], we introduced an integrated phase-field – particle swarm optimization routine to systematically identify fabrication conditions capable of producing a specified morphology, in a fully-automated fashion. This *process-to-structure* model explored the phase-space for two fabrication parameters (annealing time and substrate patterning) to identify processing paths that would result in a desired microstructure. The current work builds on these efforts in two distinct ways: (a) by introducing a more complex processing protocol, *solvent-evaporation*, alongside substrate patterning, (b) and by formulating the optimization problem centered around device *performance*, rather than microstructure; thus directly connecting the *process-to-property* relationship and providing a more comprehensive approach towards developing high-performance devices.

While the framework is generally applicable to organic electronics, our application example is focused on designing processing conditions during solution-processed fabrication of bulk-heterojunction (BHJ) *organic solar cells* that result in devices with enhanced photo-voltaic performance. The typical BHJ architecture consists of phase-separated blends of electron-donating and electron-accepting materials, leading to highly complex domain structures. Hence, the performance of these devices, especially the short-circuit current, J_{sc}, is a product of competing (microstructural) design constraints (domain size restriction for exciton dissociation, tortuosity and connectivity for charge transport, connectivity with electrodes for charge collection, among others).

We specifically link a phase-field – based morphology evolution framework [30, 42, 43] (process $\rightarrow$ structure simulator) and a graph-based morphology quantification scheme [112, 113, 114] (structure $\rightarrow$ property simulator) with an efficient, parallelized, Bayesian optimization routine. We explore how two experimentally important processing conditions can be tuned to achive imporved performance. The first, and most significant, is the rate of solvent evaporation. Naturally, when two components are diluted in a volatile common solvent, the systematic removal of this solvent via evaporation creates enrichment pockets,

triggering morphology evolution; ultimately leaving behind a binary blend at the final state. The nature of the resultant microstructure is notably dependent on the solvent type [100, 115] and evaporation profile. Building on this latter point, several studies have shown that the microstructure feature size and arrangement is highly dependent on the evaporation profile [116, 117, 118, 119]. And since this average 'domain' size is of critical interest to organic photovoltaics (OPV), the evaporation rate is a natural processing condition for our interests.

Our second processing condition involves the substrate surface chemistry and carries over from a previous work [111]. More specifically, the surface chemistry is modified to be preferentially attractive or repulsive to a specific component. In solution-processed thin film microstructures, surface chemistry is known to play a significant role throughout the evolution. Preferential wetting at the substrate and open interface can trigger surface-directed composition waves, influencing the final phase-separated morphology and often leading to surface enrichment layers [120, 121]. Imposing a tailored-pattern of alternating attractive and repulsive regions (through dip-pen nanolithography, for example) one can effectively modulate the morphology development [47, 48, 46]. Herein, we choose the surface pattern wavelength as a tunable processing condition, while fixing the amplitude, in an effort to guide the domain structures and to prevent an unfavorable enrichment layer.

The choice of these two processing conditions, evaporation rate and substrate patterning wavelength, highlights the interplay between two competing morphology control mechanisms: a top-down, evaporative effect, posed against that of a bottom-up, surface-driven influence. Further, since both are foundational features of solution processing techniques, this illustrative example has strong implications for a broad range of organic electronics.

The outline of this paper is as follows: First, we provide a brief description of the ternary, evaporation-based phase-field methodology at the core of our morphology evolution framework. Then, Section 3 is devoted to the development of several structure-based performance indicators, which directly serve as an objective function for the optimization routine. Sections 4 & 5 address the optimization routine and implementation details. Finally, Section 6 provides illustrative results from the optimization framework, followed by concluding remarks in Section 7.

3.2 Ternary phase-field model

Building on a previous work, we now formulate a ternary system for a thin film, consisting of two polymers diluted in a common solvent [30, 122]. Throughout the film processing (morphology evolution), the solvent is removed from the top boundary via evaporation, ultimately leaving behind a binary polymer blend. The phase-field model tracks the evolution of an order parameter, $\phi_i(\boldsymbol{x}, t) \in [0, 1]$, in which we assume the solution to be incompressible: $\sum_{i=p_1,p_2,s} \phi_i = 1.0$. The free energy functional for this system is defined as follows:

$$F(\phi_i) = \int_\Omega \Big[f(\phi_{p_1}, \phi_{p_2}, \phi_s) + \sum_{i=p_1,p_2} \frac{\epsilon_i^2}{2} |\nabla \phi_i|^2 \Big] d\Omega + \int_\Gamma f_s(\boldsymbol{x}, \phi)\, d\Gamma. \tag{3.1}$$

Here, $f(\phi_i)$ is the local, *homogeneous* (*bulk*) free energy of mixing, which is known to govern phase separation. This quantity which has a non-convex, double-welled profile, corresponding to the equilibrium concentrations of the separated phases. The square gradient term in Eq. 3.1 represents the *interfacial* energy, and depends on the composition gradient, scaled by the interfacial coefficient ε^2. Finally, $f_s(\boldsymbol{x}, \phi)$ introduces a spatially-dependent surface potential at the lower boundary to incorporate substrate patterning effects.

For this work, the homogeneous energy is constructed using the Flory-Huggins model [123, 55]:

$$f(\phi_i) = \Big[\sum_{p_1,p_2,s} \frac{\phi_i \ln(\phi_i)}{N_i} + \sum_{p_1,p_2,s} \sum_{j \neq i} \phi_i \phi_j \chi_{ij} \Big], \tag{3.2}$$

where, ϕ_i is the volume fraction of component i; N_i is the degree of polymerization, χ_{ij} is the Flory-Huggins binary interaction parameter between component i and j. Note, all units are considered to be dimensionless.

The surface energy component, F_s, designed to selectively introduce the effects of substrate patterning throughout the fabrication process. This is introduced through the following surface integral:

$$F_s(\boldsymbol{x}, \phi_i) = -\int_\Gamma f_s(\boldsymbol{x}, \phi_i)\, d\Gamma, \tag{3.3}$$

$$= -\int_\Gamma \Big[p_1(\mathbf{x})(h_1 \phi_{p_1} + g_1 \phi_{p_1}^2) + p_2(\mathbf{x})(h_2 \phi_{p_2} + g_2 \phi_{p_2}^2) \Big] d\Gamma. \tag{3.4}$$

The spatially-dependent function, $p_i(\boldsymbol{x}) \rightarrow \{-1, 0, 1\}$, describes the local, point-wise, nature of the surface pattern. A non-zero value, $p_i(\boldsymbol{x}) = \pm 1$, at point $\boldsymbol{x}$, indicates an *attractive* or *repulsive* surface chemistry

towards component i. Otherwise, a zero-value is imposed, indicating component neutrality. The magnitude of the surface potential is then introduced through the parameters h_i and g_i [54, 55]; in this work, $h_1 = h_2$ & $g_2 = g_2$. As in Ref. [111], the substrate patterning scheme consists of an alternating attractive/repulsive motif applied to the lower boundary as a surface flux. A simple square wave, of wavelength λ_p, is used to represent the imposed pattern[1].

Next, using the continuity relation and Fick's First Law, we formulate the governing equations. Note, we only consider for two components, since the third is implied: $\phi_s = 1 - \phi_p - \phi_f$. See Ref. [30] for more information.

$$\frac{\partial \phi_{p_1}}{\partial t} + u\frac{\partial \phi_{p_1}}{\partial h} = \nabla \cdot \left[M_{p_1} \nabla \left(\frac{\partial f(\phi_{p_1}, \phi_{p_2})}{\partial \phi_{p_1}} - \epsilon^2 \nabla^2 \phi_{p_1} \right) \right] + \xi_{p_1} \tag{3.5}$$

$$\frac{\partial \phi_{p_2}}{\partial t} + u\frac{\partial \phi_{p_2}}{\partial h} = \nabla \cdot \left[M_{p_2} \nabla \left(\frac{\partial f(\phi_{p_1}, \phi_{p_2})}{\partial \phi_{p_2}} - \epsilon^2 \nabla^2 \phi_{p_2} \right) \right] + \xi_{p_2} \tag{3.6}$$

Here, $M_i = 1$ is the species mobility of component i, which is assumed to be spatially uniform and independent of concentration. Advection term accounts for the change in height due to evaporation. The terms, ξ_{p_1} and ξ_{p_2} are Gaussian space-time white noise forcing terms, emulating thermal fluctuations. These are often referred to as *Cook* noise terms and are subject to fluctuation dissipation (FDT) constraints [124, 125]: $\langle \xi(\boldsymbol{x}, t) \rangle = 0$ and $\langle \xi(\boldsymbol{x}, t), \xi(\boldsymbol{x}', t') \rangle = 2M\nabla^2 \delta(\boldsymbol{x} - \boldsymbol{x}')\delta(t - t')$.

Finally, the solvent component, ϕ_s, is assumed to evaporate uniformly from the top surface. Hence, as the solvent is removed, the height of the system decreases with time, $\frac{\partial h}{\partial t} = -k_e \bar{\phi}_s^{top}$. Here, k_e is the evaporation rate, and $\bar{\phi}_s^{top}$ is the average content of the solvent at the top layer [30].

3.3 Graph-based morphology quantification

As described in the opening segment, crafting an appropriate cost functional is critical to producing effective results. In our previous work [111], we employed a weighted sum of morphology descriptors and image analysis tools to match a target microstructure of our choosing. In this work, we define a cost functional using *performance* descriptors, rather than structural descriptors. Hence, for applications involving

[1]Note: λ_p is normalized by a characteristic length scale for convenience, ℓ_d. In this work, we choose the final film thickness, h_{final}, as a reference scale.

OPVs, we turn to a set of physically-meaningful morphology descriptors that directly correlate to the device performance; or, for this application, the short circuit current density, J_{sc}.

The basic operating principles of OPVs, broadly speaking, may be classified into three stages: (a) light absorption and exciton creation (donor material), (b) exciton diffusion and subsequent dissociation (donor-acceptor interface), and (c) charge transport to electrodes (acceptor material). For maximal performance, it's crucial that each stage operate unimpeded, since they are co-dependent. A bottleneck at any stage may prove detrimental to the overall device performance. Taking advantage of a previously developed morphology characterization framework [112], we directly translate each stage into morphology descriptors, defined as follows[2]:

- f_{abs} - *Absorption efficiency:* Excitons generated, as a fraction of the total incident radiation. Assuming all of the donor material is available for absorption, this is simplified to the volume fraction of the donor material within the final phase-separated film.

- $f_{w\cdot diss}$ - *Exciton dissociation efficiency:* Ratio of excitons dissociated to the number of excitons generated. Following [108], we use a weighted *'distance to interface.'* For each *voxel* of the donor material, the shortest distance to interface (d_i) is computed, and then weighted by a distance, L_d (defined as the mean exciton diffusion length, $L_d \approx 10nm - 20nm$). Materials that sustain longer exciton lifetimes have numerically higher L_d compared to materials with shorter exciton lifetime. Numerically, this is represented as:

$$f_{w\cdot diss} = \frac{\sum_{i=1}^{N_{donor}} ((d_i < L_d)?\exp(-(d_i/L_d)) : 0)}{N_{donor}}, \tag{3.7}$$

  instead of

$$f_{diss} = \frac{\sum_{i=1}^{N_{donor}} ((d_i < L_d)?1 : 0)}{N_{donor}}. \tag{3.8}$$

  In this work, we define L_d in terms of the characteristic length scale: $L_d = 0.1 \cdot \ell_d$.

- f_{useful} - *Charge transport efficiency:* Ratio of charges collected at the electrodes to the total number of excitons dissociated. This is calculated as the relative fraction of interfacial area with complementary pathways to both the electrodes.

[2] *Herein, we assume: p_1 = donor material, and p_2 = acceptor material.*

Physically speaking, $f_{abs} \in [0, 1]$ represents the relative amount of donor material capable of absorbing incident radiation and producing an exciton; $f_{w\cdot diss} \in [0, 1]$ represents the relative number of excitons generated that were able to diffuse to the interface before recombining. This 'recombination length' is often on the order of 10-20 nm for realistic systems. Hence, $f_{w\cdot diss}$ takes domain size into consideration. Finally, $f_{useful} \in [0, 1]$ quantifies the relative amount of acceptor material connecting the donor-acceptor interface to the electrodes; this metric provides a natural way to penalize morphologies with islands. Further details regarding the methodology and implementation can be found elsewhere [112, 108].

Based on the findings from Wodo *et al.* [108], the performance of each microstructure, as defined by the short circuit current density, J_{sc}, maintains a direct correlation with the product of these three metrics; that is:

$$J_{sc} \approx f_{abs} \cdot f_{w\cdot diss} \cdot f_{useful}. \tag{3.9}$$

Hence, rather than actually computing the J_{sc} at every evaluation point (which is computationally intensive), we instead formulate our cost function as the following product:

$$\mathcal{F}(\phi) = f_{abs} \cdot f_{w\cdot diss} \cdot f_{useful}. \tag{3.10}$$

In which ϕ is the final, phase-separated morphology.

3.4 Bayesian optimization

Next, we pose an optimization problem to identify the appropriate fabrication conditions (evaporation rate and substrate patterning wavelength) that provide the *highest* performing OPV morphology. We select a surrogate-based optimization routine, as cost function evaluations are unavoidably expensive; Each $\mathcal{F}(\phi)$ evaluation requires a complete phase-field simulation before performing the graph-based morphology interrogation and post-processing. Depending on the system configuration (fabrication conditions) this can be immensely expensive. Thus, we seek to minimize the number of function evaluations.

To meet these ends, we select a Bayesian optimization (BO) routine. This model uses Gaussian processes to construct a surrogate cost function. Then, with every iteration, this surrogate is updated using Bayesian statistics, which continues until a termination criteria is satisfied [126, 127]. In addition to reducing the

number of function evaluations (relative to comparable global optimization routines), BO offers additional advantages; such as asynchronous iteration updates, which allows for efficient parallelization. In materials design problems, Bayesian optimization routines are well-suited and growing in popularity [128, 129]. In this work, we have employed such an asynchronous routine, custom built for deployment on large supercomputing clusters. A full description of the algorithm and implementation will be the focus of an upcoming publication.

3.5 Numerical Implementation

For this work, we assume a 1:1 blend ratio for a model system characterized by: $\chi_{12} = 1.0, \chi_{13} = \chi_{23} = 0.4$, $N_p = N_f = 5$, $N_s = 1$, with an interfacial coefficient of $\epsilon^2 = 4\text{E-}6$. Each simulation is initialized with an *identical* Gaussian-distributed random field: $\phi(\boldsymbol{x}, 0) = \phi_0 + \mathcal{N}(0, \sigma)$, in which $\sigma = 0.005$. The coupled Cahn-Hilliard equations are solved via continuous Galerkin (CG) finite elements, on two-dimensional cross-sections, consisting of 800×50 linear elements. This geometry was selected to provide a rich palette of structural features while requiring modest computational resources. The nonlinear system is solved using an in-house, finite element (FEM) framework written in C++, which utilizes a parallelized Newton-Raphson scheme provided by the PETSc solver library [60]. Each simulation was solved via 12 CPUs on the Comet cluster[3]. Solution times vary, ranging from 30 min to 4 hours, depending on the evaporation rate, among a number of other factors. Further implementation details may be found in Refs. [30, 42].

3.6 Results & Discussion

In this section, we first present a set of representative phase-field solutions and illustrate the effects of solvent evaporation rate and substrate patterning as morphology control mechanisms. Then, we perform the optimization routine and provide an in-depth discussion while exploring the phase-space. In addition, the short circuit current, J_{sc}, is computed via drift-diffusion simulations for a realistic polymer:fullerene material system. Then, to illustrate the versatility of this methodology, these results are repeated for a

[3] *Comet* is an XSEDE resource consisting of 1,944 nodes with 24 - 2.5 GHz Xeon E5-2680v3 cores per node and 124 GB of RAM.

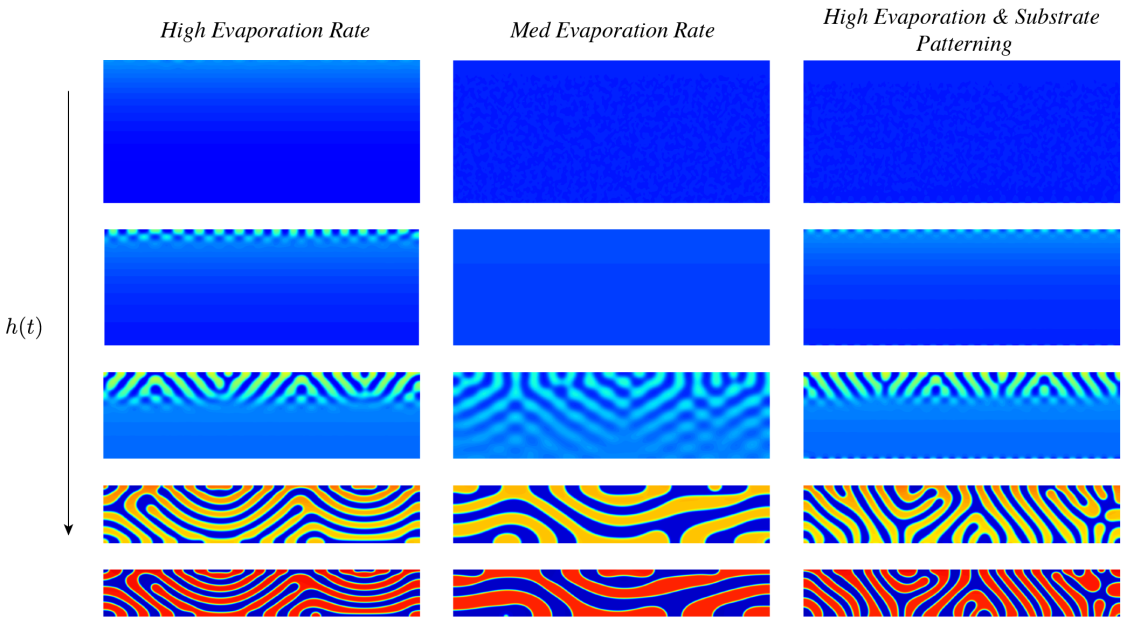

isucaption Illustrative representations of microstructural evolution and solvent evaporation; (Left) High evaporation rate ($k_e = 10$); (Center) Med. evaporation rate ($k_e = 1.0$); (Right) High evaporation rate and substrate patterning ($k_e = 1.0,\ \lambda_p = 0.2$).

system of double exciton dissociation length, that is: $2\,L_d$. Finally, we provide closing remarks and discuss future works.

3.6.1 Influence of evaporation rate & substrate patterning

In solution processing applications, solvent evaporation is the key phenomena driving phase separation. Here, solvent removal at the top surface is pitted against the mass diffusion within the film. The interplay between these competing forces significantly affects the final phase-separated morphology. High evaporation rates, in which solvent removal outpaces diffusion, leads to an early phase separation near the top surface. This produces smaller domain sizes with an affinity towards a 'layered' final structure. Alternatively, slower evaporation rates provide a more balanced phase-separation profile, leading to larger, often 'interpenetrated,' domain structures. Figure **??** provides a set of representative examples, comparing two evaporation rates, $k_e = 10$ (left) and $k_e = 1.0$ (center), which illustrates this point. A more detailed exploration is provided in Refs. [30, 43].

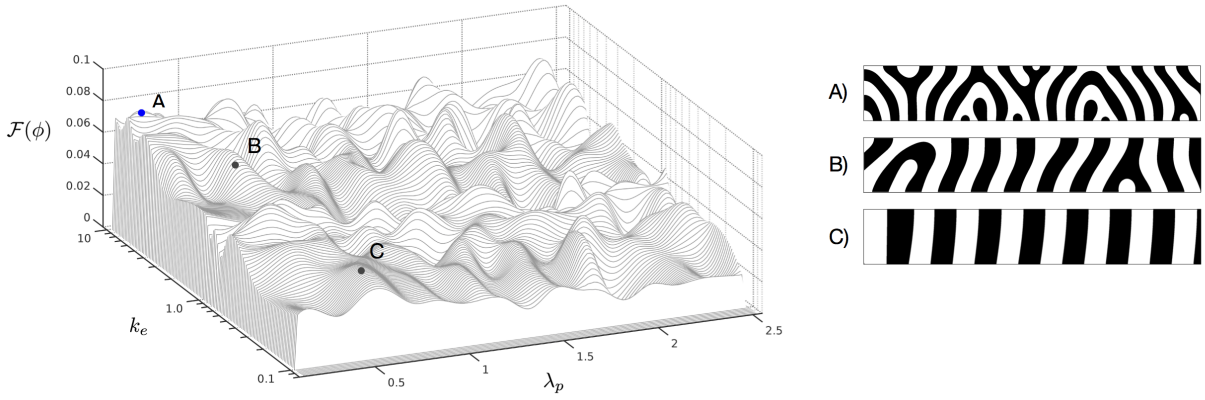

Figure 3.1: (Left) The objective function evaluated across the search space with several points of interest highlighted. Point A (blue), indicates the global maxima (optimal solution). (Right) Corresponding morphologies for points A - F (*Note: Images have been truncated for visualization purposes; only one-third of the domain length is shown*)

In addition, Figure **??** also shows the effects of substrate patterning, Figure **??** (right). While high evaporation rates often produce 'layered' microstructures, introducing a well-chosen substrate pattern can act as a guiding force throughout the evolution. As an example, Figure **??** (right) shows a high evaporation rate $k_e = 10$ with a commensurate substrate pattern. The result is a breakup of the 'layered' structure in which many domains are drawn vertical, replicating the underlying substrate pattern.

3.6.2 Optimization

We now present the results from performing the optimization. Two studies were considered, consisting of two different exciton dissociation length scales. Each optimization took approximately 60 iterations, resulting in approximately 12 hours of total computing time, before the Bayesian optimization routine converged on a global maxima.

Exciton dissociation length: L_d: The results from this first study are shown in Figure 3.1, along with several other points of interest across the phase space.[4] The global maxima, shown at point (A), consists of a number of thin, yet highly connected, domain structures. This is a result of the relatively high evaporation

[4]This surface plot is a product of 400 objective function evaluations, evenly spread across the phase space and interpolated for visualization purposes.

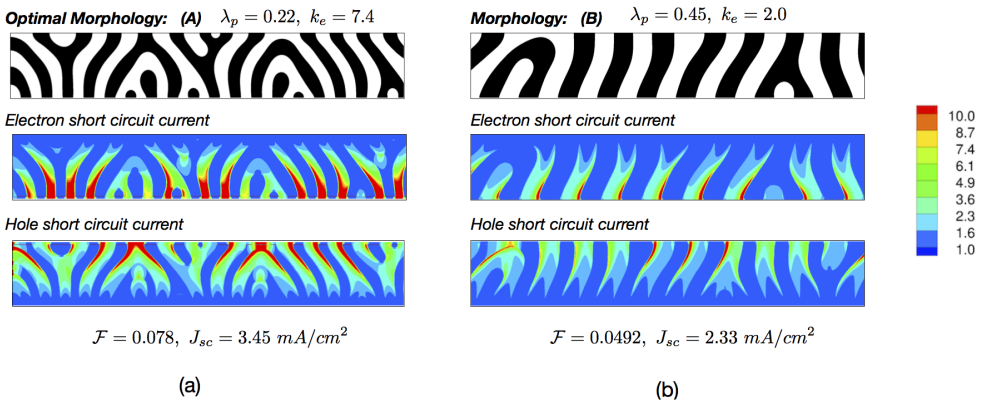

Figure 3.2: Electron and hole current densities for (a) The optimal solution predicted by the Bayesian optimization framework; and (b) Nearby, high-performing morphology.

rate as well as a narrow patterning wavelength. These spaghetti-like structures are often ideal for OPV applications: domains are relatively thin (on the order of the dissociation length scale), highly connected, and have a relatively high interfacial area. Figure 3.2 provides electron & hole current density distributions for points (A) & (B) in Figure 3.1. Here, since both morphologies have good connectivity, it's apparent that the larger domain structures are a restricting factor for point (B). This is due to the fact that domain sizes larger than the exciton dissociation length result in wasted charges. In contrast, point (F) in Figure 3.1 has several unconnected domains, resulting in a considerably lower J_{sc} of 1.20 mA/cm^2. This reveals the domain connectivity to be a significant, yet highly volatile, performance metric.

A further exploration of the phase space provides a window into the interplay between evaporation rate and substrate patterning. Comparing points A, B, & C in Figure 3.1, reveals a consistent domain growth as the evaporation rate decreases. This leads to a columnar morphology in Figure 3.1 (C), in which the columns are larger than that of the patterning wavelength, λ_p. This indicates that the characteristic domain size is largely determined by the evaporation rate and that the substrate patterning has a limited ability to direct the morphology towards a specified template. The surface patterning does, however, discourage enrichment layers and, depending on the characteristic domain size, can guide the evolution. This results

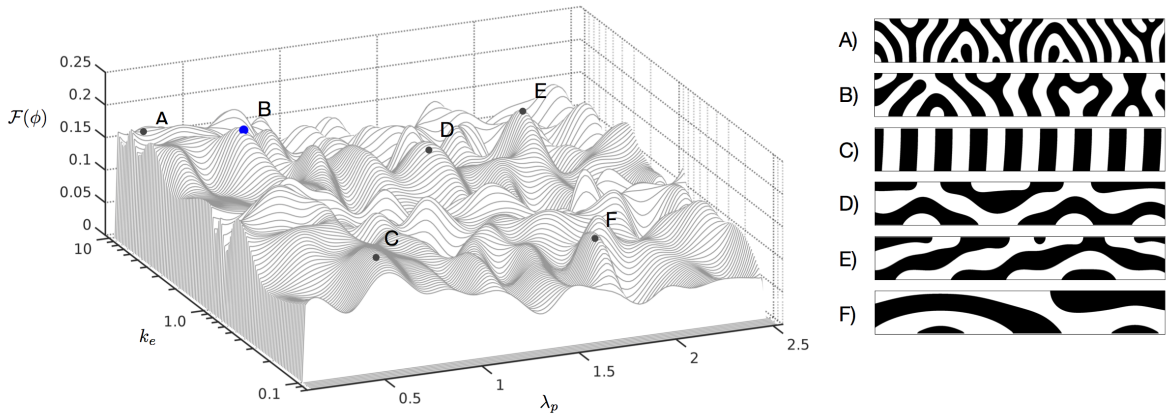

Figure 3.3: (Left) The objective function for 2 L_d. Here, point B (blue), indicates the global maxima (optimal solution). (Right) Corresponding morphologies for points A - F (*Note: Images have been truncated for visualization purposes; only one-third of the domain length is shown*)

in good connectivity, with a slight penalty for larger domain sizes - as is apparent by the *gradual* objective function decrease.

However, as the surface pattern wavelength increases, the objective function quickly becomes more volatile. The middle region of Figure 3.1, $1 \leq \lambda_p \leq 2$, reveals a strong competition between the substrate patterning and evaporation rate, leading to more complex microstructures with larger, and often stretched, domains; as shown in Figure 3.1 (D) & (E). Here, slight changes in either processing condition may result in a blocking layer or several disconnected regions, which significantly affects the performance. In contrast, the left-most region of the surface, $\lambda_p \leq 1.0$, produced smaller, yet more numerous, domain structures. As a result, the probability of large disconnected regions is low. Hence, we observe considerably less volatility in this region, with gradual changes attributed to domain size.

Exciton dissociation length: 2 L_d: Now, to showcase the versatility of this implementation, we now double the exciton dissociation length and rerun the optimization routine. The results from this experiment are shown in Figure 3.3, in which the optimal structure is now point (B), rather than (A). Now, since the dissociation length has been extended, there is less of a penalty imposed for larger domain structures. This is evident by the slight plateau in the objective function, near points (A) & (B). The gradient between

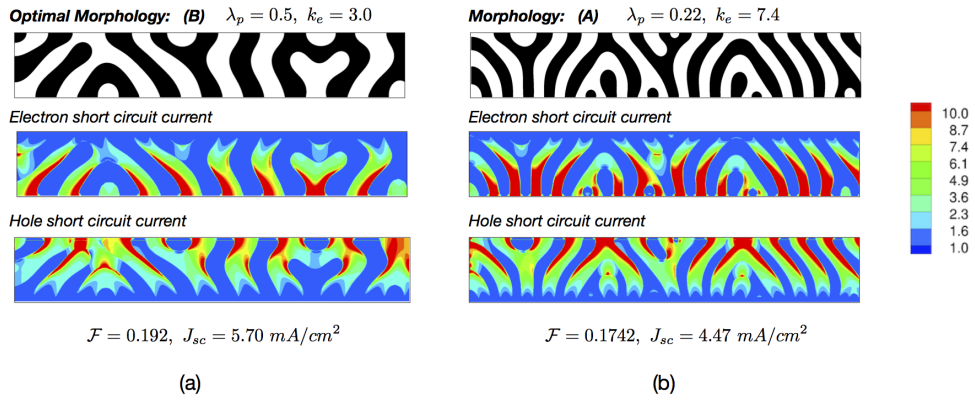

Figure 3.4: Electron and hole current densities for $2\,L_d$ simulation; (a) The predicted optimal solution for $2\,L_d$; and (b) Previous optimal solution, predicted for L_d.

points (A), (B), & (C) is comparable, but less pronounced near the ridge at $\lambda_p = 0.5$. However, for pattern wavelengths larger than this point, the objective function again becomes highly volatile. Here, the substrate pattern has a diminished ability to contain the domain structures leading to sharp changes in connectivity.

Figure 3.4 compares the charge densities for points for each optimal solution (points (A) & (B) in Figure 3.3). Now, the larger domains are clearly more favorable as there is more donor material available for (useful) charge generation. While both morphologies are high-performing, the disconnected regions in point (A) now become significant, leading to inefficiencies. Similar trends are observed throughout the phase space in Figure 3.3. Several morphologies with large, yet well connected, domain structures, that would have been penalized previously, now perform well. This is particularly true for points (C) & (F).

3.7 Conclusions

In this work, we expand upon previous efforts and present a comprehensive process–structure–property optimization framework to efficiently identify processing conditions that maximize a set of performance metrics. Herein, an efficient and scalable Bayesian optimization routine was employed to automatically identify such processing conditions. As an illustrative example, we considered OPV fabrication in which solvent evaporation and substrate patterning were presented as processing conditions. We maximize a set

of performance-based morphology descriptors that have been shown to directly correlate with OPV performance.

Our results illustrate the capacity for an automated, performance-based optimization in thin-film devices and shed light on the process–performance relationships. In particular, we observed that high evaporation rates coupled with a well-chosen substrate pattern can produce predictably high-performing microstructures.

This approach is easily generalized to a variety of performance metrics in materials science and requires minimal heuristic information by the user. This opens up the possibility of an efficient, automated, and rational identification of processing conditions to produce optimal morphologies. Future works will expand to more realistic materials systems, in which more variables may be considered.

CHAPTER 4. CONCLUSIONS AND FUTURE WORK

In this work, a general methodology has been presented, which provides a scalable and extensible approach towards the rational design for tailored microstructures with enhanced functionalities. More specifically, the contributions may be summarized as follows:

- *Developed and employed predictive modeling framework* for the fabrication of thin film organic electronic devices. This phase-field–based, finite element framework was written in C++ to model binary and ternary phase-separation and solvent evaporation for a wide range of material parameters and processing conditions.

- *Explored the process-structure-property relationships* governing OE device behavior. The above framework was used to explore the complex relationships between each linkage, that is, process-to-microstructure as well as the process-to-property linkage.

- *Developed and implemented optimization framework* to automatically link process-to-structure and process-to-performance and systematically identify promising processing conditions. This includes developing a microstructure-sensitive objective function for each case.

Furthermore, behind each of these contributions lies a set of well-documented, computational tools that may be used to a study broad range of problems.

4.1 Future Work

Future works will expand on these contributions to include:

- *Additional fabrication techniques.* This work emphasized thermal annealing, solvent evaporation, and substrate patterning. Introducing shear forces into the framework will allow for more realistic solutions.

- *Additional system components*. Several realistic polymer systems often include additives or multiple components. Adding these into the framework may provide an interesting solution space to explore.

- *Crystallization.* Many polymers of considerable interest are known to crystalize during fabrication. Including a Cahn-Allen equation to account for the crystalized phases would be significantly more attuned to state-of-the-art polymer electronic devices.

- *Expand to larger, more realistic materials systems.* In this work, on the basis of computational limitations, several simplifications were made; namely:

    i) Only *'model systems'* were explored since real material properties require considerably more computing resources and are generally difficult to find proper values in the literature. Experimental collaborators may be able to find such realistic material properties which would have considerably more impact.

    ii) A limited, two-dimensional computational domain size was considered. The choice of this domain can result in a vastly different outcomes. Future work should consider *thin vs. thick films, 2D vs. 3D, & etc.*

A final future work is to release the above set of well-documented, computational tools to the public (*i.e.,* on GitHub for example). This would have considerable value and utility for a number of groups studying similar problems - particularly the experimental community.

CHAPTER 5. BIBLIOGRAPHY

[1] Tsuyoshi Sekitani, Hiroyoshi Nakajima, Hiroki Maeda, Takanori Fukushima, Takuzo Aida, Kenji Hata, and Takao Someya. Stretchable active-matrix organic light-emitting diode display using printable elastic conductors. *Nature materials*, 8(6):494–499, 2009.

[2] Mihai Irimia-Vladu, Eric D Głowacki, Gundula Voss, Siegfried Bauer, and Niyazi Serdar Sariciftci. Green and biodegradable electronics. *Materials Today*, 15(7):340–346, 2012.

[3] Anke Teichler, Jolke Perelaer, and Ulrich S Schubert. Inkjet printing of organic electronics–comparison of deposition techniques and state-of-the-art developments. *Journal of Materials Chemistry C*, 1(10):1910–1925, 2013.

[4] Ying Diao, Leo Shaw, Zhenan Bao, and Stefan CB Mannsfeld. Morphology control strategies for solution-processed organic semiconductor thin films. *Energy & Environmental Science*, 7(7):2145–2159, 2014.

[5] Yiqiang Zhan, Yongfeng Mei, and Lirong Zheng. Materials capability and device performance in flexible electronics for the internet of things. *Journal of Materials Chemistry C*, 2(7):1220–1232, 2014.

[6] Takao Someya, Zhenan Bao, and George G Malliaras. The rise of plastic bioelectronics. *Nature*, 540(7633):379–385, 2016.

[7] Daniel T Simon, Erik O Gabrielsson, Klas Tybrandt, and Magnus Berggren. Organic bioelectronics: bridging the signaling gap between biology and technology. *Chem. Rev*, 116(21):13009–13041, 2016.

[8] Stefano Lai, Alessandra Zucca, Piero Cosseddu, Francesco Greco, Virgilio Mattoli, and Annalisa Bonfiglio. Ultra-conformable organic field-effect transistors and circuits for epidermal electronic applications. *Organic Electronics*, 46:60–67, 2017.

[9] Takao Someya, Tsuyoshi Sekitani, Shingo Iba, Yusaku Kato, Hiroshi Kawaguchi, and Takayasu Sakurai. A large-area, flexible pressure sensor matrix with organic field-effect transistors for artificial skin applications. *Proceedings of the National Academy of Sciences of the United States of America*, 101(27):9966–9970, 2004.

[10] Tomoyuki Yokota, Peter Zalar, Martin Kaltenbrunner, Hiroaki Jinno, Naoji Matsuhisa, Hiroki Kitanosako, Yutaro Tachibana, Wakako Yukita, Mari Koizumi, and Takao Someya. Ultraflexible organic photonic skin. *Science advances*, 2(4):e1501856, 2016.

[11] Sungwon Lee, Amir Reuveny, Jonathan Reeder, Sunghoon Lee, Hanbit Jin, Qihan Liu, Tomoyuki Yokota, Tsuyoshi Sekitani, Takashi Isoyama, Yusuke Abe, et al. A transparent bending-insensitive pressure sensor. *Nature nanotechnology*, 11(5):472–478, 2016.

[12] Yasser Khan, Aminy E. Ostfeld, Claire M. Lochner, Adrien Pierre, and Ana C. Arias. Monitoring of Vital Signs with Flexible and Wearable Medical Devices. *Advanced Materials*, 28(22):4373–4395, 2016.

[13] National Research Council (US). Committee on Integrated Computational Materials Engineering. *Integrated Computational Materials Engineering: A transformational discipline for improved competitiveness and national security*. National Academies Press, 2008.

[14] Jitesh H Panchal, Surya R Kalidindi, and David L McDowell. Key computational modeling issues in integrated computational materials engineering. *Computer-Aided Design*, 45(1):4–25, 2013.

[15] B. Crone, A. Dodabalapur, Y.-Y. Lin, R.W. Filas, Z. Bao, A. LaDuca, R. Sarpeshkar, H.E. Katz, and W. Li. Large-scale complementary integrated circuits based on organic transistors. *Nature*, 403(6769):521–523, 2000.

[16] Christos D Dimitrakopoulos and Debra J Mascaro. Organic thin-film transistors: A review of recent advances. *IBM Journal of research and development*, 45(1):11–27, 2001.

[17] Harald Hoppe and Niyazi Serdar Sariciftci. Organic solar cells: An overview. *Journal of Materials Research*, 19(7):1924–1945, 2004.

[18] Christoph Brabec, Ullrich Scherf, and Vladimir Dyakonov. *Organic photovoltaics: materials, device physics, and manufacturing technologies*. John Wiley & Sons, 2011.

[19] Howard A Stone. Ice-phobic surfaces that are wet. *ACS Nano*, 6(8):6536–6540, 2012.

[20] Liang Zhao, Yong-Sheng Hu, Hong Li, Zhaoxiang Wang, and Liquan Chen. Porous li4ti5o12 coated with n-doped carbon from ionic liquids for li-ion batteries. *Advanced Materials*, 23(11):1385–1388, 2011.

[21] Byeong-Heon Jeong, Eric MV Hoek, Yushan Yan, Arun Subramani, Xiaofei Huang, Gil Hurwitz, Asim K Ghosh, and Anna Jawor. Interfacial polymerization of thin film nanocomposites: A new concept for reverse osmosis membranes. *Journal of Membrane Science*, 294(1):1–7, 2007.

[22] Charles Featherston and Eoin O'Sullivan. A Review of International Public Sector Strategies and Roadmaps: A Case Study in Advanced Materials. Technical report, Centre for Science Technology and Innovation, Institute for Manufacturing, University of Cambridge, 2014.

[23] (National Science and Technology Council, 2011). *Materials Genome Initiative for Global Competitiveness*, 2011. http://www.whitehouse.gov/sites/default/files/microsites/ostp/materials_genome_initiative-final.pdf.

[24] Surya R. Kalidindi, David B. Brough, Shengyen Li, Ahmet Cecen, Aleksandr L. Blekh, Faical Yannick P. Congo, and Carelyn Campbell. Role of materials data science and informatics in accelerated materials innovation. *MRS Bulletin*, 41(08):596–602, 2016.

[25] Surya R Kalidindi, Andrew J Medford, and David L McDowell. Vision for data and informatics in the future materials innovation ecosystem. *JOM*, 68(8):2126–2137, 2016.

[26] Romain Quey, PR Dawson, and Fabrice Barbe. Large-scale 3d random polycrystals for the finite element method: Generation, meshing and remeshing. *Computer Methods in Applied Mechanics and Engineering*, 200(17):1729–1745, 2011.

[27] Hamad F. Alharbi and Surya R. Kalidindi. Crystal plasticity finite element simulations using a database of discrete Fourier transforms. *International Journal of Plasticity*, 66:71–84, 2015.

[28] Shankar Ganapathysubramanian and Nicholas Zabaras. Modeling the thermoelastic-viscoplastic response of polycrystals using a continuum representation over the orientation space. *International Journal of Plasticity*, 21(1):119–144, 2005.

[29] Shahriyar Keshavarz and Somnath Ghosh. Multi-scale crystal plasticity finite element model approach to modeling nickel-based superalloys. *Acta Materialia*, 61(17):6549–6561, 2013.

[30] Olga Wodo and Baskar Ganapathysubramanian. Modeling morphology evolution during solvent-based fabrication of organic solar cells. *Computational Materials Science*, 55:113–126, apr 2012.

[31] Jian Qin, Gurdaman S. Khaira, Yongrui Su, Grant P. Garner, Marc Miskin, Heinrich M. Jaeger, and Juan J. de Pablo. Evolutionary pattern design for copolymer directed self-assembly. *Soft Matter*, 9(48):11467, 2013.

[32] Sangmin Lee and Veera Sundararaghavan. Multi-scale modeling of moving interface problems with flux and field jumps: Application to oxidative degradation of ceramic matrix composites. *International Journal for Numerical Methods in Engineering*, 85(6):784–804, 2011.

[33] Veera Sundararaghavan and Nicholas Zabaras. Design of microstructure-sensitive properties in elasto-viscoplastic polycrystals using multi-scale homogenization. *International Journal of Plasticity*, 22(10):1799–1824, 2006.

[34] David T Fullwood, Stephen R Niezgoda, Brent L Adams, and Surya R Kalidindi. Microstructure sensitive design for performance optimization. *Progress in Materials Science*, 55(6):477–562, 2010.

[35] Weihua Li and Marcus Müller. Directed self-assembly of block copolymers by chemical or topographical guiding patterns: Optimizing molecular architecture, thin-film properties, and kinetics. *Progress in Polymer Science*, 54:47–75, 2016.

[36] Gurdaman S. Khaira, Jian Qin, Grant P. Garner, Shisheng Xiong, Lei Wan, Ricardo Ruiz, Heinrich M. Jaeger, Paul F. Nealey, and Juan J. De Pablo. Evolutionary optimization of directed self-assembly of triblock copolymers on chemically patterned substrates. *ACS Macro Letters*, 3(8):747–752, 2014.

[37] Martin Kaltenbrunner, Matthew S White, Eric D Głowacki, Tsuyoshi Sekitani, Takao Someya, Niyazi Serdar Sariciftci, and Siegfried Bauer. Ultrathin and lightweight organic solar cells with high flexibility. *Nature Communications*, 3:770, 2012.

[38] Chizu Sekine, Yoshiaki Tsubata, Takeshi Yamada, Makoto Kitano, and Shuji Doi. Recent progress of high performance polymer oled and opv materials for organic printed electronics. *Science and Technology of Advanced Materials*, 15(3):034203, 2014.

[39] Kenjiro Fukuda, Yasunori Takeda, Makoto Mizukami, Daisuke Kumaki, and Shizuo Tokito. Fully solution-processed flexible organic thin film transistor arrays with high mobility and exceptional uniformity. *Scientific Reports*, 4:3947, 2014.

[40] Takao Someya, Yusaku Kato, Tsuyoshi Sekitani, Shingo Iba, Yoshiaki Noguchi, Yousuke Murase, Hiroshi Kawaguchi, and Takayasu Sakurai. Conformable, flexible, large-area networks of pressure and thermal sensors with organic transistor active matrixes. *Proceedings of the National Academy of Sciences of the United States of America*, 102(35):12321–12325, 2005.

[41] Takao Someya, Zhenan Bao, and George G. Malliaras. The rise of plastic bioelectronics. *Nature*, 540(7633):379–385, 2016.

[42] Olga Wodo and Baskar Ganapathysubramanian. Computationally efficient solution to the cahn-hilliard equation: Adaptive implicit time schemes, mesh sensitivity analysis and the 3d isoperimetric problem. *Journal of Computational Physics*, 230(15):6037–6060, 2011.

[43] Olga Wodo and Baskar Ganapathysubramanian. How do evaporating thin films evolve? unravelling phase-separation mechanisms during solvent-based fabrication of polymer blends. *Applied Physics Letters*, 105(15):153104, 2014.

[44] Harald Hoppe, Michael Niggemann, Christoph Winder, Jürgen Kraut, Renate Hiesgen, Andreas Hinsch, Dieter Meissner, and Niyazi Serdar Sariciftci. Nanoscale morphology of conjugated polymer/fullerene-based bulk-heterojunction solar cells. *Advanced Functional Materials*, 14(10):1005–1011, 2004.

[45] Youngkyoo Kim, Stelios A. Choulis, Jenny Nelson, Donal D. C. Bradley, Steffan Cook, and James R. Durrant. Device annealing effect in organic solar cells with blends of regioregular poly (3–hexylthiophene) and soluble fullerene. *Applied Physics Letters*, 86(6):1–3, 2005.

[46] Lee Y Park, Andrea M Munro, and David S Ginger. Controlling film morphology in conjugated polymer: fullerene blends with surface patterning. *Journal of the American Chemical Society*, 130(47):15916–15926, 2008.

[47] Georg Krausch. Surface induced self assembly in thin polymer films. *Materials Science and Engineering: R: Reports*, 14(1):v–94, 1995.

[48] Martin Böltau, Stefan Walheim, Jürgen Mlynek, Georg Krausch, and Ullrich Steiner. Surface-induced structure formation of polymer blends on patterned substrates. *Nature*, 391(6670):877–879, 1998.

[49] Mark Geoghegan and Georg Krausch. Wetting at polymer surfaces and interfaces. *Progress in Polymer Science*, pages 261–302, 2003.

[50] Joseph H Wei, David C Coffey, and David S Ginger. Nucleating pattern formation in spin-coated polymer blend films with nanoscale surface templates. *The Journal of Physical Chemistry B*, 110(48):24324–24330, 2006.

[51] Kui Zhao, Olga Wodo, Dingding Ren, Hadayat Ullah Khan, Muhammad Rizwan Niazi, Hanlin Hu, Maged Abdelsamie, Ruipeng Li, Er Li, Liyang Yu, et al. Vertical phase separation in small molecule: Polymer blend organic thin film transistors can be dynamically controlled. *Advanced Functional Materials*, 2016.

[52] C Schaefer, PPAM van der Schoot, and JJ Michels. Structuring of polymer solutions upon solvent evaporation. *Physical Review E*, 91(2):022602, 2015.

[53] Daniel Schwen, Larry K Aagesen, John W Peterson, and Michael R Tonks. Rapid multiphase-field model development using a modular free energy based approach with automatic differentiation in moose/marmot. *Computational Materials Science*, 132:36–45, 2017.

[54] Richard AL Jones, Edward J Kramer, Miriam H Rafailovich, Jonathon Sokolov, and Steven A Schwarz. Surface enrichment in an isotopic polymer blend. *Physical Review Letters*, 62(3):280–283, 1989.

[55] Richard Anthony Lewis Jones. *Polymers at surfaces and interfaces*. Cambridge University Press, 1999.

[56] A. Karim, J. F. Douglas, B. P. Lee, S. C. Glotzer, J. A. Rogers, R. J. Jackman, E. J. Amis, and G. M. Whitesides. Phase separation of ultrathin polymer-blend films on patterned substrates. *Phys. Rev. E*, 57:R6273–R6276, Jun 1998.

[57] Benjamin P. Lee, Jack F. Douglas, and Sharon C. Glotzer. Filler-induced composition waves in phase-separating polymer blends. *Phys. Rev. E*, 60:5812–5822, Nov 1999.

[58] L Kielhorn and M Muthukumar. Phase separation of polymer blend films near patterned surfaces. *The Journal of Chemical Physics*, 111(5):2259–2269, 1999.

[59] Yingrui Shang, David Kazmer, Ming Wei, Joey Mead, and Carol Barry. Numerical simulation of phase separation of immiscible polymer blends on a heterogeneously functionalized substrate. *The Journal of chemical physics*, 128(22):224909, 2008.

[60] E. Arge, A. M. Bruaset, and H. P. Langtangen, editors. *Efficient Management of Parallelism in Object Oriented Numerical Software Libraries*. Birkhäuser Press, 1997.

[61] Adam F. Hannon, Yi Ding, Wubin Bai, Caroline A. Ross, and Alfredo Alexander-Katz. Optimizing topographical templates for directed self-assembly of block copolymers via inverse design simulations. *Nano Letters*, 14(1):318–325, 2014.

[62] Salvatore Torquato. *Random heterogeneous materials: microstructure and macroscopic properties*, volume 16. Springer Science & Business Media, 2013.

[63] Olga Wodo, Srikanta Tirthapura, Sumit Chaudhary, and Baskar Ganapathysubramanian. A graph-based formulation for computational characterization of bulk heterojunction morphology. *Organic Electronics*, 13(6):1105–1113, 2012.

[64] Zhou Wang, Alan Conrad Bovik, Hamid Rahim Sheikh, and Eero P. Simoncelli. Image quality assessment: From error visibility to structural similarity. *IEEE Transactions on Image Processing*, 13(4):600–612, 2004.

[65] Mehul P Sampat, Zhou Wang, Shalini Gupta, Alan Conrad Bovik, and Mia K Markey. Complex wavelet structural similarity: A new image similarity index. *IEEE transactions on image processing*, 18(11):2385–2401, 2009.

[66] Lin Zhang, Lei Zhang, Xuanqin Mou, and David Zhang. Fsim: A feature similarity index for image quality assessment. *IEEE transactions on Image Processing*, 20(8):2378–2386, 2011.

[67] KR Elder, TM Rogers, and RC Desai. Early stages of spinodal decomposition for the Cahn-Hilliard-Cook model of phase separation. *Physical Review B*, 38(7), 1988.

[68] Aleksij Aksimentiev, Krzysztof Moorthi, and Robert Holyst. Scaling properties of the morphological measures at the early and intermediate stages of the spinodal decomposition in homopolymer blends. *The Journal of Chemical Physics*, 112(13):6049, 2000.

[69] Alan J Bray. Theory of phase-ordering kinetics. *Advances in Physics*, 51(2):481–587, 2002.

[70] MATLAB. *version 9.1.0 (R2016b)*. The MathWorks Inc., Natick, Massachusetts, 2016.

[71] A. J. Kulkarni, K. Krishnamurthy, S. P. Deshmukh, and R. S. Mishra. Microstructural optimization of alloys using a genetic algorithm. *Materials Science and Engineering A*, 372(1–2):213–220, 2004.

[72] Héctor Gómez, Victor M Calo, Yuri Bazilevs, and Thomas JR Hughes. Isogeometric analysis of the cahn-hilliard phase-field model. *Computer Methods in Applied Mechanics and Engineering*, 197(49):4333–4352, 2008.

[73] Marcio Gameiro, Konstantin Mischaikow, and Thomas Wanner. Evolution of pattern complexity in the cahn-hilliard theory of phase separation. *Acta Materialia*, 53(3):693–704, feb 2005.

[74] Wufeng Xue, Lei Zhang, Xuanqin Mou, and Alan C. Bovik. Gradient magnitude similarity deviation: A highly efficient perceptual image quality index. *IEEE Transactions on Image Processing*, 23(2):668–695, 2014.

[75] Fred W Glover and Gary A Kochenberger. *Handbook of metaheuristics*, volume 57. Springer Science & Business Media, 2006.

[76] Dan Simon. *Evolutionary optimization algorithms*. John Wiley & Sons, 2013.

[77] R. Eberhart and J. Kennedy. A new optimizer using particle swarm theory. *Proceedings of the Sixth International Symposium on Micro Machine and Human Science*, pages 39–43, 1995.

[78] J Kennedy and R Eberhart. Particle swarm optimization. *Proceedings of IEEE International Conference on Neural Networks*, 4:1942–1948, 2002.

[79] Riccardo Poli. An analysis of publications on particle swarm optimisation applications. *Journal of Artificial Evolution and Applications*, 2008(2):1–57, 2007.

[80] Y Del Valle, G K Venayagamoorthy, S Mohagheghi, J C Hernandez, and R G Harley. Particle swarm optimization: Basic concepts, variants and applications in power systems. *IEEE Transactions on Evolutionary Computation*, 12(2):171–195, 2008.

[81] Gang Li, Vishal Shrotriya, Jinsong Huang, Yan Yao, Tom Moriarty, Keith Emery, and Yang Yang. High-efficiency solution processable polymer photovoltaic cells by self-organization of polymer blends. *Nature materials*, 4(11):864–868, 2005.

[82] Lukas Schmidt-Mende, Andreas Fechtenkötter, Klaus Müllen, Ellen Moons, Richard H Friend, and JD MacKenzie. Self-organized discotic liquid crystals for high-efficiency organic photovoltaics. *Science*, 293(5532):1119–1122, 2001.

[83] Yutaka Matsuo, Yoshiharu Sato, Takaaki Niinomi, Iwao Soga, Hideyuki Tanaka, and Eiichi Nakamura. Columnar structure in bulk heterojunction in solution-processable three-layered pin organic photovoltaic devices using tetrabenzoporphyrin precursor and silylmethyl [60] fullerene. *Journal of the American Chemical Society*, 131(44):16048–16050, 2009.

[84] Ji Sun Moon, Jae Kwan Lee, Shinuk Cho, Jiyun Byun, and Alan J Heeger. "columnlike" structure of the cross-sectional morphology of bulk heterojunction materials. *Nano Letters*, 9(1):230–234, 2008.

[85] Michael Graetzel, René AJ Janssen, David B Mitzi, and Edward H Sargent. Materials interface engineering for solution-processed photovoltaics. *Nature*, 488(7411):304–312, 2012.

[86] J. Xue, B.âĂL'P. Rand, S. Uchida, and S.âĂL'R. Forrest. A hybrid planar-mixed molecular heterojunction photovoltaic cell. *Advanced Materials*, 17(1):66–71, 2005.

[87] Mariano Campoy-Quiles, Toby Ferenczi, Tiziano Agostinelli, Pablo G Etchegoin, Youngkyoo Kim, Thomas D Anthopoulos, Paul N Stavrinou, Donal DC Bradley, and Jenny Nelson. Morphology evolution via self-organization and lateral and vertical diffusion in polymer: fullerene solar cell blends. *Nature Materials*, 7(2):158–164, 2008.

[88] Youngkyoo Kim, Steffan Cook, Sachetan M Tuladhar, Stelios A Choulis, Jenny Nelson, James R Durrant, Donal DC Bradley, Mark Giles, Iain McCulloch, Chang-Sik Ha, et al. A strong regioregularity effect in self-organizing conjugated polymer films and high-efficiency polythiophene: fullerene solar cells. *Nature Materials*, 5(3):197–203, 2006.

[89] Sophie E. Gledhill, Brian Scott, and Brian A. Gregg. Organic and nano-structured composite photovoltaics: An overview. *Journal of Materials Research*, 20(12):3167–3179, 2005.

[90] Gavin A Buxton and Nigel Clarke. Computer simulation of polymer solar cells. *Modelling and simulation in Materials Science and Engineering*, 15(2):13, 2006.

[91] Biswajit Ray and Muhammad A Alam. Random vs regularized opv: Limits of performance gain of organic bulk heterojunction solar cells by morphology engineering. *Solar Energy Materials and Solar Cells*, 99:204–212, 2012.

[92] M. Shah and V. Ganesan. Correlations between morphologies and photovoltaic properties of rod- coil block copolymers. *Macromolecules*, 43(1):543–552, 2009.

[93] Hari K. Kodali and Baskar Ganapathysubramanian. A computational framework to investigate charge transport in heterogeneous organic photovoltaic devices. *Computer Methods in Applied Mechanics and Engineering*, 247:113–129, 2012.

[94] Hari K. Kodali and Baskar Ganapathysubramanian. Computer simulation of heterogeneous polymer photovoltaic devices. *Modelling and Simulation in Materials Science and Engineering*, 20(3):035015, 2012.

[95] C. R. McNeill, S. Westenhoff, C. Groves, R. H. Friend, and N. C. Greenham. Influence of nanoscale phase separation on the charge generation dynamics and photovoltaic performance of conjugated polymer blends: Balancing charge generation and separation. *The Journal of Physical Chemistry C*, 111(51):19153–19160, 2007.

[96] P Cyganik, Andrzej Bernasik, Andrzej Budkowski, B Bergues, K Kowalski, Jakub Rysz, J Lekki, M Lekka, and Z Postawa. Phase decomposition in polymer blend films cast on substrates patterned with self-assembled monolayers. *Vacuum*, 63(1):307–313, 2001.

[97] Stephen R Forrest. The path to ubiquitous and low-cost organic electronic appliances on plastic. *Nature*, 428(6986):911–918, 2004.

[98] Joseph S Chang, Antonio F Facchetti, and Robert Reuss. A circuits and systems perspective of organic/printed electronics: Review, challenges, and contemporary and emerging design approaches. *IEEE Journal on Emerging and Selected Topics in Circuits and Systems*, 7(1):7–26, 2017.

[99] Christoph J Brabec, Srinivas Gowrisanker, Jonathan JM Halls, Darin Laird, Shijun Jia, and Shawn P Williams. Polymer–fullerene bulk-heterojunction solar cells. *Advanced Materials*, 22(34):3839–3856, 2010.

[100] Harald Hoppe and Niyazi Serdar Sariciftci. Morphology of polymer/fullerene bulk heterojunction solar cells. *Journal of Materials Chemistry*, 16(1):45–61, 2006.

[101] Matthew S White, Martin Kaltenbrunner, Eric D Głowacki, Kateryna Gutnichenko, Gerald Kettlgruber, Ingrid Graz, Safae Aazou, Christoph Ulbricht, Daniel AM Egbe, Matei C Miron, et al. Ultrathin, highly flexible and stretchable pleds. *Nature Photonics*, 7(10):811–816, 2013.

[102] Seung Hyun Sung and Bryan W Boudouris. Systematic control of the nanostructure of semiconducting-ferroelectric polymer composites in thin film memory devices. *ACS Macro Letters*, 4(3):293–297, 2015.

[103] Seungwon Lee, Hyejeong Seong, Sung Gap Im, Hanul Moon, and Seunghyup Yoo. Organic flash memory on various flexible substrates for foldable and disposable electronics. *Nature Communications*, 8(1):725, 2017.

[104] Se-Hee Kim, Keun-Ho Choi, Sung-Ju Cho, Sinho Choi, Soojin Park, and Sang-Young Lee. Printable solid-state lithium-ion batteries: a new route toward shape-conformable power sources with aesthetic versatility for flexible electronics. *Nano letters*, 15(8):5168–5177, 2015.

[105] Mariano Campoy-Quiles, Toby Ferenczi, Tiziano Agostinelli, Pablo G Etchegoin, Youngkyoo Kim, Thomas D Anthopoulos, Paul N Stavrinou, Donal DC Bradley, and Jenny Nelson. Morphology evolution via self-organization and lateral and vertical diffusion in polymer: fullerene solar cell blends. *Nature materials*, 7(2):158–164, 2008.

[106] C Schaefer, Jasper J Michels, and PPAM van der Schoot. Structuring of thin-film polymer mixtures upon solvent evaporation. *Macromolecules*, 49(18):6858–6870, 2016.

[107] Stefano Curtarolo, Gus LW Hart, Marco Buongiorno Nardelli, Natalio Mingo, Stefano Sanvito, and Ohad Levy. The high-throughput highway to computational materials design. *Nature materials*, 12(3):191–201, 2013.

[108] Olga Wodo, Jaroslaw Zola, Balaji Sesha Sarath Pokuri, Pengfei Du, and Baskar Ganapathysubramanian. Automated, high throughput exploration of process–structure–property relationships using the mapreduce paradigm. *Materials Discovery*, 1:21–28, 2015.

[109] Akash Gupta, Ahmet Cecen, Sharad Goyal, Amarendra K Singh, and Surya R Kalidindi. Structure–property linkages using a data science approach: application to a non-metallic inclusion/steel composite system. *Acta Materialia*, 91:239–254, 2015.

[110] David B Brough, Daniel Wheeler, James A Warren, and Surya R Kalidindi. Microstructure-based knowledge systems for capturing process-structure evolution linkages. *Current Opinion in Solid State and Materials Science*, 21(3):129–140, 2017.

[111] Spencer Pfeifer, Olga Wodo, and Baskar Ganapathysubramanian. An Optimization Approach to Identify Processing Pathways for Achieving Tailored Thin Film Morphologies. *Computational Materials Science*, 2017.

[112] Olga Wodo, Srikanta Tirthapura, Sumit Chaudhary, and Baskar Ganapathysubramanian. Computational characterization of bulk heterojunction nanomorphology. *Journal of Applied Physics*, 112(6):064316, 2012.

[113] Olga Wodo, John D. Roehling, Adam J. Moulé, and Baskar Ganapathysubramanian. Quantifying organic solar cell morphology: a computational study of three-dimensional maps. *Energy & Environmental Science*, 6(10):3060, 2013.

[114] Balaji Sesha Sarath Pokuri, Joseph Sit, Olga Wodo, Derya Baran, Tayebeh Ameri, Christoph J. Brabec, Adam J. Moule, and Baskar Ganapathysubramanian. Nanoscale Morphology of Doctor Bladed versus Spin-Coated Organic Photovoltaic Films. *Advanced Energy Materials*, 1701269:1701269, 2017.

[115] Kenji Kawano, Jun Sakai, Masayuki Yahiro, and Chihaya Adachi. Effect of solvent on fabrication of active layers in organic solar cells based on poly (3-hexylthiophene) and fullerene derivatives. *Solar Energy Materials and Solar Cells*, 93(4):514–518, 2009.

[116] K Dalnoki-Veress, JA Forrest, JR Stevens, and JR Dutcher. Phase separation morphology of spin-coated polymer blend thin films. *Physica A: Statistical Mechanics and its Applications*, 239(1-3):87–94, 1997.

[117] Andrzej Budkowski, Andrzej Bernasik, P Cyganik, J Raczkowska, B Penc, B Bergues, K Kowalski, Jakub Rysz, and J Janik. Substrate-determined shape of free surface profiles in spin-cast polymer blend films. *Macromolecules*, 36(11):4060–4067, 2003.

[118] Sandra Kouijzer, Jasper J Michels, Mauricio van den Berg, Veronique S Gevaerts, Mathieu Turbiez, Martijn M Wienk, and René AJ Janssen. Predicting morphologies of solution processed polymer: fullerene blends. *J. Am. Chem. Soc*, 135(32):12057–12067, 2013.

[119] Jacobus J van Franeker, Daniel Westhoff, Mathieu Turbiez, Martijn M Wienk, Volker Schmidt, and René AJ Janssen. Controlling the dominant length scale of liquid–liquid phase separation in spin-coated organic semiconductor films. *Advanced Functional Materials*, 25(6):855–863, 2015.

[120] Cecilia M Björström, Svante Nilsson, Andrzej Bernasik, Andrzej Budkowski, Mats Andersson, Kjell O Magnusson, and Ellen Moons. Vertical phase separation in spin-coated films of a low bandgap polyfluorene/pcbm blend-effects of specific substrate interaction. *Applied Surface Science*, 253(8):3906–3912, 2007.

[121] C Schaefer, JJ Michels, and PPAM van der Schoot. Dynamic surface enrichment in drying thin-film binary polymer solutions. *Macromolecules*, 50(15):5914–5919, 2017.

[122] Junseok Kim and Kyungkeun Kang. A numerical method for the ternary cahn–hilliard system with a degenerate mobility. *Applied Numerical Mathematics*, 59(5):1029–1042, 2009.

[123] Lloyd M Robeson. *Polymer blends*. Hanser, 2007.

[124] Sharon C. Glotzer. Computer simulations of spinodal decomposition in polymer blends. In *Annual Reviews of Computational Physics II*, pages 1–46. World Scientific, 1995.

[125] Alain Karma and Wouter-Jan Rappel. Phase-field model of dendritic sidebranching with thermal noise. *Physical review E*, 60(4):3614, 1999.

[126] H-M Gutmann. A radial basis function method for global optimization. *Journal of Global Optimization*, 19(3):201–227, 2001.

[127] Eric Brochu, Vlad M Cora, and Nando De Freitas. A tutorial on bayesian optimization of expensive cost functions, with application to active user modeling and hierarchical reinforcement learning. *arXiv preprint arXiv:1012.2599*, 2010.

[128] Diana M Negoescu, Peter I Frazier, and Warren B Powell. The knowledge-gradient algorithm for sequencing experiments in drug discovery. *INFORMS Journal on Computing*, 23(3):346–363, 2011.

[129] Shenghong Ju, Takuma Shiga, Lei Feng, Zhufeng Hou, Koji Tsuda, and Junichiro Shiomi. Designing nanostructures for phonon transport via bayesian optimization. *Physical Review X*, 7(2):021024, 2017.